https://doi.org/10.5194/egusphere-2026-3392
Preprint. Discussion started: 24 August 2026

Vertical responses of urban heat islands to heatwaves and their local climate zones dependence: a case study of Guangzhou, China

Fu Luo[1], Yuanjian Yang[1], Ting Sun[2], Zuofang Zheng[3], Xueyan Bi[4], Guoyu Ren[5], and Simone Lolli[6]

[1]Collaborative Innovation Centre on Forecast and Evaluation of Meteorological Disasters, School of Atmospheric Physics, Nanjing University of Information Science and Technology, Nanjing, China
[2]Department of Risk and Disaster Reduction, University College London, London, UK
[3]Institute of Urban Meteorology, China Meteorological Administration, Beijing, China
[4]Institute of Tropical and Marine Meteorology, Guangzhou, China
[5]Department of Atmospheric Science, School of Environmental Studies, China University of Geosciences, Wuhan, China
[6]CNR-IMAA, Contrada S. Loja, 85050 Tito Scalo (PZ), Italy

Correspondence: Yuanjian Yang (yyj1985@nuist.edu.cn)

Abstract. The interaction between urban heat island (UHI) and heatwaves (HWs) shapes urban extreme heat, but whether HW-induced UHI amplification reorganises canopy-to-boundary-layer thermal structure, and whether local climate zones (LCZs) modulate this response, remains unclear. Here, we investigated two July 2020 HW events in the Guangzhou metropolitan area in southern China, using 1 km LCZ-coupled Weather Research and Forecasting (WRF) simulations. We analysed the vertical thermal response of the urban area and individual LCZs using canopy and boundary-layer UHI intensities (CUHII, BUHII), layer-mean urban–rural air-temperature differences (Layer ΔT), and surface-energy-balance and turbulence indicators. HWs amplified both CUHII and BUHII in a vertically non-uniform manner: CUHII increased more than BUHII, and additional warming concentrated in the canopy and lower boundary layer. Warming propagated upward as the daytime boundary layer developed but contracted toward the surface at night and during transition periods, with upper-level responses weakening or reversing. LCZ heterogeneity was largely confined to the lowest ~250 m: LCZ 1 showed the strongest additional warming, LCZ 2 and LCZ 4 reached comparable levels through different energy–turbulence pathways, and LCZ 6 was weakest. Stronger sensible heat flux, higher Bowen ratios, sustained nocturnal heat sources, and reduced low-level stability jointly drove this diurnal reorganisation. During HW1, residual-layer warm anomalies in LCZ 1 (0.41 °C at 500–600 m) persisted through the night and provided an additional heat reservoir for next-day mixed-layer development, whereas LCZ 6 showed much weaker memory effects. HW2 reproduced the inter-LCZ ranking with weaker absolute amplitude.

1 Introduction

Under global warming, heatwaves (HWs), periods of intense heat that persist for days or weeks, have become increasingly frequent (Meehl and Tebaldi, 2004; IPCC, 2018; Kotharkar and Ghosh, 2021) and exert pronounced impacts on public health and on social and ecological systems (WMO and WHO, 2016; Tan et al., 2007; Robine et al., 2007). Nearly 60 % of the world's population now lives in cities, and urbanisation effects, particularly the urban heat island (UHI) phenomenon, have become an important driver of regional-scale warming (Shi et al., 2011; Schlünzen et al., 2023). The UHI refers to the phenomenon

https://doi.org/10.5194/egusphere-2026-3392
Preprint. Discussion started: 24 August 2026

whereby the centre of an urban or metropolitan area is warmer than surrounding rural areas. HWs, which are usually synoptic large-scale phenomena, in urban areas tend to amplify the UHI, and the amplified UHI in turn aggravates urban extreme heat and the associated exposure and risk during HWs. The combined influence of HWs and the UHI on urban extreme heat risk, and the synergy between the two, therefore cannot be neglected.

Previous studies have documented HW–UHI synergy in many cities worldwide and shown that its sign (positive or negative) and magnitude depend primarily on the background climate and on differences in the urban–rural surface energy partitioning response during HWs (Li and Bou-Zeid, 2013; Zhao et al., 2014; Li et al., 2016; Sun et al., 2017). On the one hand, UHI intensity (UHII) is generally enhanced during HWs, accompanied by deteriorated ventilation, increased heat storage, and suppressed evaporative cooling (Ao et al., 2019; Jiang et al., 2019; Luo et al., 2023; Park and Baik, 2026). On the other hand, some studies have observed no amplification or even declining trend in UHII during HW periods, which imply that climate differences or changes in soil moisture have certain impact on HW–UHI interaction (Chew et al., 2021; Richard et al., 2021) because differences in the background climate contribute significantly to changes in UHII (Zhao et al., 2014). In general, HW–UHI synergy is governed by a variety of factors and involves nonlinear interactions between the two, among which differences in surface energy partitioning play a key role (Kong et al., 2021).

Most previous studies on HW–UHI synergy have focused on surface or canopy-level temperatures (Li et al., 2016; Jiang et al., 2019; Kabisch et al., 2023), whereas the planetary boundary layer (PBL), the key layer through which surface thermal anomalies propagate upward and interact with the synoptic background, has received considerably less attention. Recent studies have begun to investigate the thermal structure, heat budget, turbulence, and advection within the PBL during HWs (Xin et al., 2024; Huang et al., 2025; Tang et al., 2025). However, most of these studies treated the city as a single entity and overlooked the differential modulation of vertical thermal-anomaly transfer by intra-urban morphological heterogeneity. How the upward extension and vertical organisation of urban thermal anomalies under HW conditions are modulated by different surface types thus remains an open question. Simultaneously, recent research has begun to extend its scope from surface heat-storage processes to larger spatio-temporal scales. Sun et al. (2017) showed that heat storage is the dominant component of the urban surface energy-budget response during HWs. Li et al. (2024) further used a global climate model to demonstrate that the high thermal inertia of urban impervious materials causes urban air temperatures to exhibit stronger persistence at synoptic scales than rural air temperatures. These studies advanced the understanding of HW–UHI synergy from instantaneous energy partitioning to multi-day thermal persistence, but their analyses remained largely confined to the surface or near-surface layer. From the perspective of urban boundary-layer physics, the residual layer formed after the daytime collapse of the convective boundary layer can retain the thermal characteristics of the previous day's mixed layer overnight and be re-entrained by the newly developing boundary layer the following morning (Stull, 1988), constituting a potential boundary-layer-scale thermal-memory mechanism. Whether this residual-layer thermal memory is amplified under HW conditions, and how it is modulated by urban morphology, has not yet been examined.

Traditional urban classifications typically rely on rather coarse categories. Stewart and Oke (2012) introduced the concept of local climate zones (LCZs), which divides urban surfaces into 10 basic classes based on surface properties, three-dimensional structure, and human activity. The LCZ scheme effectively captures urban-landscape heterogeneity (Yang et al., 2024) and

https://doi.org/10.5194/egusphere-2026-3392
Preprint. Discussion started: 24 August 2026

provides a unified framework for characterising it. A substantial body of LCZ-based literature has confirmed that urban building morphology exerts strong control on canopy-level thermal heterogeneity (Ngarambe et al., 2020; Zong et al., 2021; Tian et al., 2023; Yang et al., 2025). LCZs with compact buildings and poor ventilation generally exhibit stronger canopy UHII and more pronounced HW–UHI synergy, whereas LCZs with open built environments tend to have weaker heat-storage capacity and are more sensitive to changes in the wind field. In addition, Weather Research and Forecasting (WRF) simulations driven by LCZ data have demonstrated that incorporating urban morphology can effectively improve the accuracy of urban air-temperature simulations (Ching et al., 2018; Brousse et al., 2016; Molnár et al., 2019; Chen et al., 2025). More recently, several studies began to use LCZ-coupled WRF simulations to analyse UHII characteristics; for example, Li et al. (2026) showed for the Guangdong–Hong Kong–Macao Greater Bay Area that LCZ 1 generally exhibited the highest UHII, highlighting the heat-storage effect of compact urban forms. Existing LCZ-based studies, however, concentrated on UHII variations at the surface or in the near-surface layer, and there remains a lack of work connecting canopy and boundary-layer UHIs and their vertical structures using an LCZ framework.

Building on these foundations, this study focuses on the Guangzhou metropolitan area in subtropical southern China and examines the HW events of July 2020. We investigated whether the vertical evolution of the canopy UHII (CUHII) and boundary-layer UHII (BUHII) under HW conditions exhibited features of continuity and disruption, and whether such vertical features showed spatial heterogeneity from an LCZ perspective. Here, "continuity" refers to the situation in which the HW-induced additional warming (i.e. the extra increment of the urban–rural air temperature difference during HWs) extends upward from the near-surface layer into higher portions of the PBL, while "disruption" refers to a marked weakening, stagnation, or even reversal of this additional warming at certain heights or times. Specifically, this study addressed the following questions: (1) Compared with non-heatwave (NHW) periods, how HWs amplified the CUHII and BUHII over the urban area as a whole and over individual LCZs, and what the corresponding vertical differences were; (2) whether the vertical transfer of this amplification effect exhibited a clear LCZ dependence in terms of continuity or disruption, and whether different LCZs influenced the persistence of residual-layer thermal memory by modulating the coupling between the nocturnal stable boundary layer and the residual layer; and (3) how the continuity or disruption of this vertical transfer across LCZs was related to differences in surface energy partitioning and to the resulting differences in turbulence and stability. The remainder of this paper is organised as follows. Section 2 introduces the data and methods; Section 3 evaluates the simulation performance and analyses the vertical thermal response; Section 4 discusses the novelty and limitations of the results; and Section 5 presents the main conclusions.

2 Data and methods

2.1 Study area

The Guangzhou metropolitan area (Guangdong Provincial Development and Reform Commission, 2023) is located in southern China, in the central part of the Guangdong–Hong Kong–Macao Greater Bay Area. It comprises mainly Guangzhou and Foshan, together with parts of Zhaoqing and Qingyuan; within this region, the present study focuses on the Guangzhou–Foshan core (Fig. 1a–b). The terrain is higher in the northeast and lower in the southwest, with hills dominating the northern and

https://doi.org/10.5194/egusphere-2026-3392
Preprint. Discussion started: 24 August 2026

eastern regions, whereas plains and terraces dominate the southern and western portions. Located along the subtropical coast and influenced by the subtropical high, the South China Sea monsoon, and low-pressure systems, the region experiences warm and humid conditions and abundant solar radiation throughout the year. Rapid urbanisation expanded the built-up area of Guangzhou to more than 1300 km^2 in 2020 (Guangzhou Municipal Planning and Natural Resources Bureau, 2021), with a permanent population of 18.68 million (The People' s Government of Guangzhou Municipality, 2021) and an impervious-surface fraction in the central urban area reaching 80–99 % (Kuang et al., 2024). Previous studies have shown that both the frequency of HWs and UHII over this region exhibit intensifying trends (Luo et al., 2023; Wang et al., 2021). Furthermore, the urban morphology of the Guangzhou metropolitan area is highly heterogeneous, with pronounced LCZ contrasts, making it well suited for testing whether thermal anomalies associated with different LCZs can be transported upward in a coherent manner. Focusing on a representative HW period over the Guangzhou metropolitan area is therefore both regionally representative and well placed to highlight the modulation of the boundary-layer thermal environment by high-density urban surfaces.

2.2 Observational data and urban morphology datasets

Hourly 2 m air temperature observations from automatic weather stations (AWSs; http://data.cma.cn/en) were used in this study. The observational data were quality-controlled by removing stations with a missing-data ratio greater than 5 % and discarding anomalously low or high values, leaving 73 stations in total. Temperatures were then corrected for elevation using the recorded station altitudes and a lapse rate of -0.006 °C m^{-1}, which was close to the standard environmental lapse rate (Stull, 1988) and within the range of near-surface lapse rates observed across mainland China (Li et al., 2013). Because the built-up areas of several cities within the Guangzhou metropolitan area are spatially contiguous, partitioning the region by administrative boundaries would interrupt this spatial continuity. We therefore identified the main built-up area by combining the AWS information with the 2020 30 m annual China Land Cover Dataset (CLCD; Yang and Huang, 2021, 2026). As shown in Fig. 1c, the resulting main built-up area encompassed Guangzhou, Foshan, and the adjacent built-up areas of Zhongshan, Dongguan, and Shenzhen, and was used to define the innermost (D03) WRF simulation domain. The AWSs used for evaluation against the simulated 2 m air temperatures are also indicated in the figure. The default MODIS land-cover data in WRF (Fig. 2b–c) were replaced with the WUDAPT 100 m global LCZ dataset (Demuzere et al., 2022b) using the w2w tool (Demuzere et al., 2022a). Each AWS was then mapped onto the LCZ grid using a nearest-neighbour algorithm to identify its LCZ type. The harmonised planetary boundary layer height dataset of Guo et al. (2022) (methodology: Guo et al. 2024) was further used to evaluate the planetary boundary layer height (PBLH) simulated by WRF. This dataset has a temporal resolution of 3 h and a spatial resolution of 0.25°.

Vertical profiles of temperature and wind were additionally evaluated against the NOAA National Centers for Environmental Information Integrated Global Radiosonde Archive Version 2 (IGRA v2; Durre et al., 2016) at Qingyuan station (WMO 59280; 23.71° N, 113.08° E), which lies within D03. The July 2020 IGRA subset contained 53 sounding times. After applying the temporal screening described in Sect. 2.5.1 and matching the soundings to the available WRF output, 41 profiles at 08:00 and 20:00 BJT during 6–29 July were retained for evaluation. Because Qingyuan is outside the urban core, this comparison was used to evaluate the regional background vertical structure and the representation of PBL processes, while the urban near-surface

https://doi.org/10.5194/egusphere-2026-3392
Preprint. Discussion started: 24 August 2026

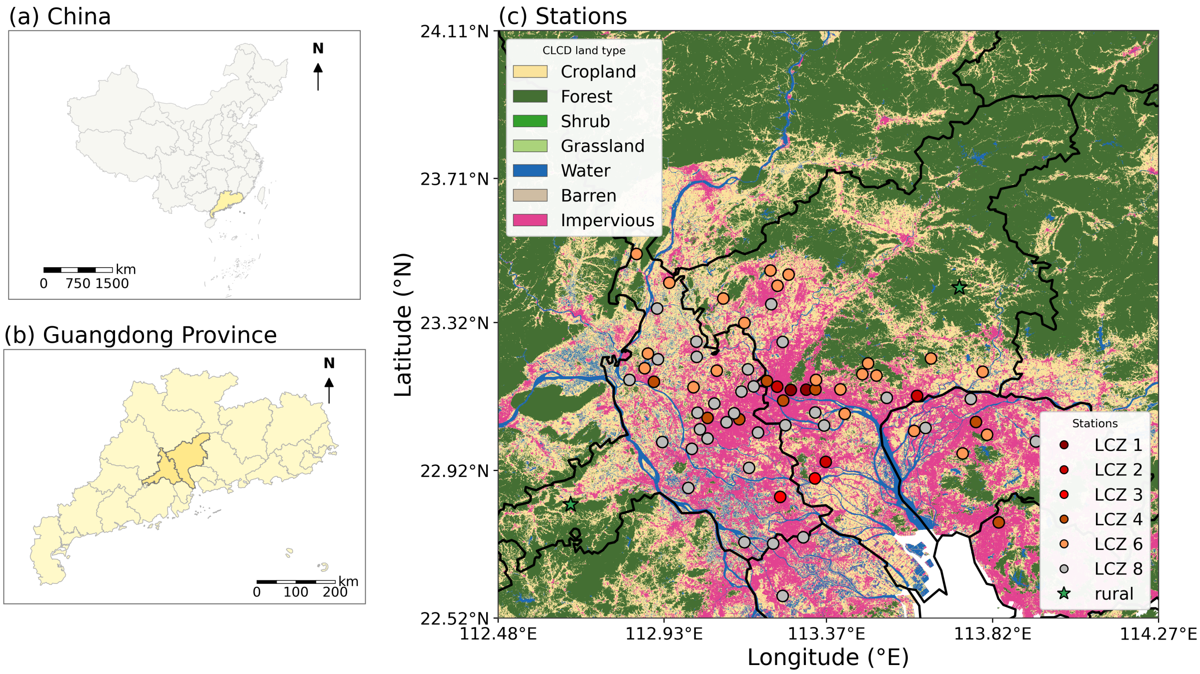

Figure 1. (a–b) Geographical location of Guangdong Province in China and of Guangzhou and Foshan within Guangdong. (c) Land-cover types of the study area derived from the CLCD dataset, with the boundary of the main built-up area (black contour), the innermost (D03) WRF simulation domain, and the 73 automatic weather stations (AWSs) used in this study, colour-coded by LCZ type. Green stars indicate the rural reference stations.

state and PBLH remained constrained by the AWS and harmonised PBLH evaluations described above. For each sounding time, WRF temperature, earth-relative horizontal wind components, and geopotential height were extracted from the nearest D03 grid cell and interpolated to the observed pressure levels using pressure as the vertical coordinate. The u and v components were interpolated before wind speed and direction were calculated. Bias, mean absolute error (MAE) and root mean square error (RMSE) were calculated from all valid sounding-level–time pairs for temperature and wind speed at pressures ≥ 50 hPa; circular bias and circular MAE were used for wind direction. For the mean-profile comparison, each sounding was interpolated to 15 common pressure levels from 1000 to 300 hPa. Mean profiles were then calculated for the full evaluation period and for the three analysis windows defined in Sect. 2.5.1.

2.3 Model configuration and experimental design

Numerical simulations were performed using WRF v4.4 (Skamarock et al., 2019) in a three-domain nested configuration with horizontal grid spacings of 9, 3, and 1 km. The domains were centred at (23.103° N, 113.201° E) (Fig. 2a) and contained 292 × 284, 295 × 241, and 184 × 178 grid points in the east–west and north–south directions, respectively. Forty vertical levels were used, with the model top set at 50 hPa. The NCEP FNL 0.25° operational global analysis (National Centers for

https://doi.org/10.5194/egusphere-2026-3392
Preprint. Discussion started: 24 August 2026

Table 1. WRF model configuration.

Physics scheme	Case 1	Case 2	Case 3	Case 4	Case 5
Microphysics	Purdue Lin	Purdue Lin	Purdue Lin	Purdue Lin	Purdue Lin
Shortwave radiation	RRTMG	RRTMG	RRTMG	RRTMG	RRTMG
Longwave radiation	RRTMG	RRTMG	RRTMG	RRTMG	RRTMG
Surface layer	Eta similarity	Eta similarity	Eta similarity	Eta similarity	Eta similarity
Land surface	Noah	Noah	Noah	Noah	Noah
Planetary boundary layer	MYJ	MYJ	MYJ	MYJ	BouLac
Urban surface	BEP	BEP–BEM	BEP & LCZ	BEP–BEM & LCZ	BEP–BEM & LCZ
Cumulus parameterization	Kain–Fritsch (only D01)	Kain–Fritsch (only D01)	Kain–Fritsch (only D01)	Kain–Fritsch (only D01)	Kain–Fritsch (only D01)

Environmental Prediction, National Weather Service, NOAA, U.S. Department of Commerce, 2015) provided the initial and lateral boundary conditions. The complete model configuration is summarised in Table 1. The physics suite combined the Purdue Lin microphysics scheme, the RRTMG longwave and shortwave radiation schemes, the Noah land-surface model, the MYJ and BouLac planetary boundary layer schemes (compared in parallel), the Eta similarity surface-layer scheme, and a multi-layer urban canopy model. We first held the PBL scheme fixed at MYJ and compared the performance of two urban canopy schemes, BEP and BEP–BEM. BEP (Building Effect Parameterization) treats buildings as drag and radiation-trapping elements but does not represent indoor energy processes (Martilli et al., 2002). BEP–BEM extends BEP by coupling a building energy model (BEM) that explicitly resolves indoor–outdoor heat exchange and waste heat from air conditioning, thereby providing a more complete representation of anthropogenic heat fluxes (Salamanca et al., 2010). For each canopy scheme, simulations were conducted with both the MODIS and LCZ land-cover datasets to compare canopy-scheme performance under different surface representations. The best-performing combination of canopy scheme and land-cover dataset was then used to compare the MYJ and BouLac PBL schemes.

2.4 Definition of urban, rural, and LCZ analysis windows

To highlight the urban signal, a rectangular window covering 23–23.3° N and 113–113.4° E was defined as the central urban region (CUR) for analysis (the black solid box in Fig. 2b–c), based on Fig. 1c. The CUR covers the core urban areas of Guangzhou and Foshan. Two rural reference areas were also selected, one to the southwest and one to the northeast of the built-up area. Each rural reference area was constructed from a 3 × 3 candidate window centred on a rural reference station (the black stars in Fig. 2c). Within this neighbourhood, grid cells were required not to be adjacent to built-up areas or water bodies, and qualifying cells were required to share the dominant underlying surface type with that of the station, forming a connected patch of at least four grid cells. After this screening, the two rural reference areas together contained 11 grid

https://doi.org/10.5194/egusphere-2026-3392
Preprint. Discussion started: 24 August 2026

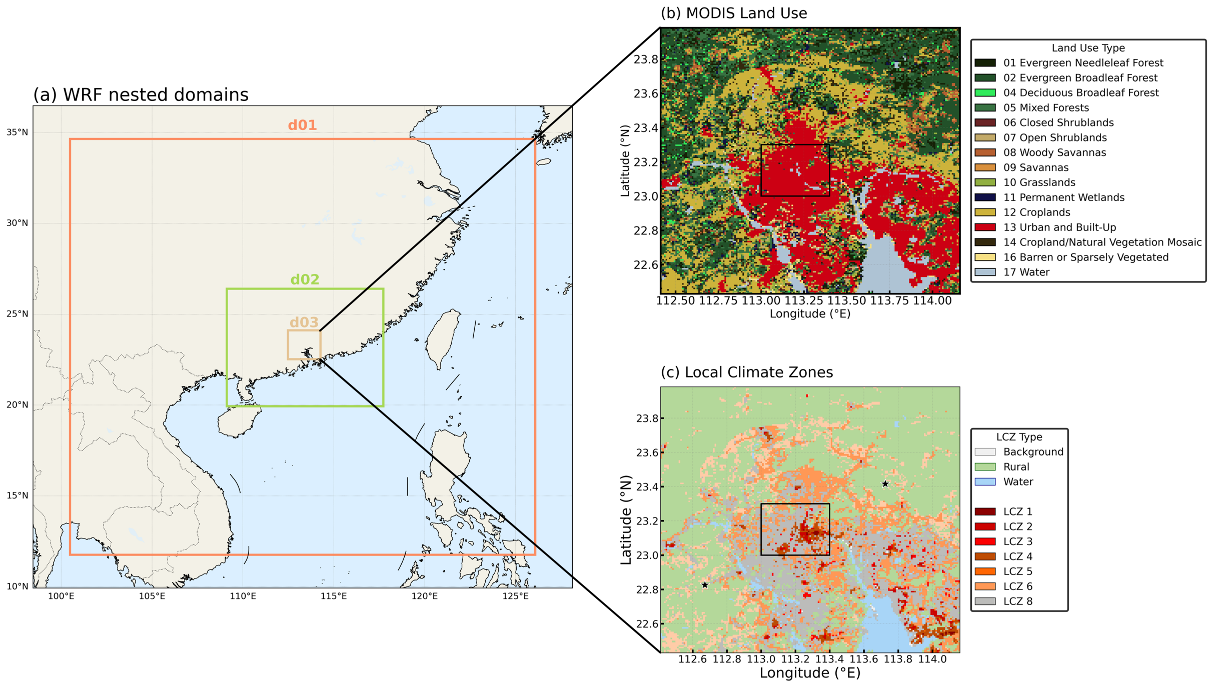

Figure 2. (a) Nested WRF simulation domains (D01, D02, and D03 at 9, 3, and 1 km horizontal grid spacing, respectively). (b) MODIS land-use categories and (c) LCZ land-use categories within D03. The black solid box in (b) and (c) marks the central urban region (CUR) used for analysis.

cells. LCZ samples were further screened within the CUR. Candidate grid cells of each LCZ were first extracted within the CUR; an 8-neighbourhood rule was then applied to remove all mixed cells immediately adjacent to rural areas, water bodies, LCZ 9 and 10, or the CUR boundary. An 8-connected component labelling was subsequently applied to each LCZ, retaining only core patches with sufficient connectivity. The aim was to keep within-class samples that were relatively homogeneous, morphologically continuous, and unaffected by edge mixing, so as to enhance the interpretability of inter-LCZ comparisons of vertical thermal response. After the screening, 8 connected grid cells were retained for LCZ 1 in the city centre (see Fig. S3 in the Supplement). LCZ 2 had 26 grid cells, distributed mainly around LCZ 1. LCZ 4 surrounded LCZ 1 and LCZ 2 and contained 82 grid cells. LCZ 3 cells were sparse and largely isolated and were therefore not considered in detail in this study. LCZ 6 was distributed around the periphery of the city centre. LCZ 8 contained the largest number of grid cells and was closer to the CUR-mean state; it was therefore used as a background reference in the subsequent analysis. Overall, the LCZs analysed in this study were LCZ 1, 2, 4, 6, and 8, which represented compact high-rise, compact midrise, open high-rise, open low-rise, and large low-rise built-up areas, respectively.

https://doi.org/10.5194/egusphere-2026-3392
Preprint. Discussion started: 24 August 2026

2.5 Heatwave identification and thermal metrics

2.5.1 Heatwave identification and case selection

Following the high-temperature threshold definition adopted by the China Meteorological Administration, a HW event was defined as a period of three or more consecutive days with daily maximum air temperature $\geq$ 35 °C. Regional HW events were identified from the AWS 2 m air temperature, while subsequent diagnostic analyses were based on the model output. The detection algorithm first identified, on a station-by-station basis, the days on which the daily maximum temperature reached the threshold; the proportion of stations meeting the threshold across the study area was then calculated for each day. A day was classified as a regional hot day if more than 50 % of the stations met or exceeded the threshold, and three consecutive regional hot days constituted one HW event. The simulation period extended from 1 to 31 July 2020, with the first five days used for spin-up. Two HW events were identified during this period (HW1: 12–16 July; HW2: 23–29 July), together with a preceding non-heatwave (NHW) period (6–11 July). According to the Guangdong–Hong Kong–Macao climate bulletin, July 2020 was relatively hot, and the HW periods were dominated by the subtropical high. Both historical weather records and the AWS observations indicated that precipitation occurred over the study area at the end of the month. Therefore, 30 and 31 July were excluded from the analysis. To ensure that the NHW and HW periods were comparable in terms of sample length and simulation reliability, a 3-day window with the most stable performance was adopted. Specifically, 6–8 July (3 days) was selected as the NHW period and the three hottest days of the first HW event (13–15 July, 3 days) were used for the HW analysis. Supplementary results for the HW2 period (24–26 July) are provided in Figs. S7–S19 and Table S1.

2.5.2 Definition of UHI metrics

The CUHII was defined as the difference between the 2 m air temperature averaged over the urban grid cells within the CUR and that averaged over the rural reference grid cells, and was taken to represent the canopy-layer heat island intensity (Eq. (1)).

$$\text{CUHII} = T2m_{\text{Urban}} - T2m_{\text{Rural}} \tag{1}$$

The vertical BUHII was defined as follows (Eq. (2–3)):

$$\text{BUHII}(t) = \frac{1}{H_c(t) - z_0} \int_{z_0}^{H_c(t)} \left[T_u(z,t) - T_r(z,t)\right] dz \tag{2}$$

$$H_c(t) = \min(\text{PBLH}_u(t), \text{PBLH}_r(t)) \tag{3}$$

Here, the subscript u denotes either the urban area as a whole or an individual LCZ, and r denotes the rural reference area; z_0 = 30 m represents the height of the “above-canopy layer”. BUHII was integrated up to the lower of the urban and rural PBLH

https://doi.org/10.5194/egusphere-2026-3392
Preprint. Discussion started: 24 August 2026

at each time step (the common dynamic boundary-layer top H_c(t)) and was defined as the thickness-weighted mean of the temperature-difference profile between z_0 and H_c(t). This metric represented the mean heat-island intensity across the entire boundary layer. Because the urban–rural PBLH difference was not consistent between the HW and NHW periods, a uniform static upper limit had clear limitations. The present dynamic definition prevented the artificial damping of upward thermal anomaly propagation associated with an overly low static limit, while simultaneously excluding temperature anomalies above the actual PBL top that an excessively high static limit would capture.

The vertical propagation structure was additionally characterised using fixed-height layer-mean urban–rural air temperature differences (Layer ΔT). This metric was a structural diagnostic of upward propagation of thermal anomalies and improved comparability across times and across LCZs. Below the common dynamic boundary-layer top, Layer ΔT could be regarded as the UHII of each individual layer. The layers analysed in this study were 2 m, 30–100 m, 100–250 m, 250–500 m, and 500–1000 m. The HW–NHW difference of ΔT (denoted $\Delta\Delta T$) was then used to characterise the additional warming during HWs, that is, the extra temperature increment introduced by the HW. A layer with $\Delta\Delta T < 0$ was regarded as showing a disruption in the upward propagation of HW-induced additional warming.

2.6 Surface energy balance

The classical urban surface energy balance equation (Oke, 2002; Oke et al., 2017) was adopted (Eq. (4)):

$$Q^* + Q_F = Q_H + Q_E + \Delta Q_S + Q_A \tag{4}$$

Here, Q^* is the net radiation, Q_F the anthropogenic heat flux, Q_H and Q_E the sensible and latent heat fluxes, ΔQ_S the change in heat storage of the surface and buildings, and Q_A the horizontal advection term. These energy components were obtained directly or indirectly from the WRF output. Q^* was computed as the difference between the downward and upward shortwave fluxes (variables SWDNB and SWUPB) and the downward and upward longwave fluxes (variables LWDNB and LWUPB). Q_H and Q_E were taken directly from the WRF output variables HFX and LH, with upward fluxes defined as positive. The Bowen ratio was defined as $Q_\mathrm{H}/Q_\mathrm{E}$ and was calculated only during the daytime when $Q^* > 0$ in order to avoid spurious values associated with very small nocturnal Q_E. ΔQ_S was approximated by the WRF ground heat flux output (variable GRDFLX), hereafter denoted Q_G, which represented the heat flux into the substrate beneath the natural-surface fraction of each grid cell. Heat storage in building walls, roofs, and indoor air was handled internally by the BEP–BEM scheme but was not output as a separate flux. Q_G therefore provided a partial-but-directionally-consistent proxy for the heat-storage term in the subsequent analysis. Q_F was estimated as a residual term (Kato and Yamaguchi, 2005; Zhou et al., 2012) and was meaningful only under the BEP–BEM configuration; its interpretation in the following sections was therefore kept conservative. As a closure check, Q_F over the rural reference area was used as a baseline: a near-zero rural residual (Fig. 10e) supported interpreting the non-zero urban residual as a genuine signal of unresolved building physical processes (Sect. 3.4.1). To assess the magnitude of Q_A, an equivalent heat flux of near-surface horizontal sensible-heat advection was computed from the wind and temperature fields at the lowest model level as $Q_\mathrm{A} \approx \rho c_p z_\mathrm{m} \left(u\frac{\partial T}{\partial x} + v\frac{\partial T}{\partial y} \right)$, where z_m was the centre height of the lowest model layer ($\approx$ 26 m).

The results showed that during the NHW period the daily peak Q_A over the CUR was about 20–25 W m^{-2}, which was only ∼10 % of the contemporaneous daytime sensible heat flux (with similar results for the HW period). This indicated that, under the quasi-stationary background associated with subtropical-high control, horizontal advection had a limited influence on the surface energy budget of the study area, and Q_A was therefore neglected in the subsequent analysis. It should be noted that this was an approximate diagnostic of near-surface sensible-heat advection only and did not include latent-heat advection or other components.

2.7 Turbulence and stability diagnostics

To describe how the surface energy components were converted into boundary-layer warming, the turbulence kinetic energy (TKE) and the gradient Richardson number (Ri) were selected as the main diagnostic indicators, complemented by PBLH as a measure of the mixing-layer depth. TKE reflects the intensity of turbulent velocity fluctuations, while Ri quantifies the relative magnitudes of buoyancy and wind shear; both are widely used in urban PBL studies (Stull, 1988; Rotach et al., 2005; Seidel et al., 2012).

The TKE budget equation is given by (Eq. (5)) (Stull, 1988):

$$\frac{\partial e}{\partial t} = P_s + P_b + T_e - \varepsilon \tag{5}$$

Here, e denotes the turbulence kinetic energy, P_s the shear production term, P_b the buoyant production or destruction term, T_e the turbulent transport term, and ε the dissipation term. An increase (decrease) in TKE implied enhanced (suppressed) vertical exchange and turbulent transport, so that the layer concerned mixed more (less) readily with the layers above and below.

The gradient Richardson number is defined as (Eq. (6–7)):

$$\mathrm{Ri} = \frac{\frac{g}{\theta_v}\frac{\partial \theta_v}{\partial z}}{\left(\frac{\partial U}{\partial z}\right)^2 + \left(\frac{\partial V}{\partial z}\right)^2} \tag{6}$$

$$\theta_v = \theta\,(1 + 0.61 q_v) \tag{7}$$

where θ_v is the virtual potential temperature, U and V are the horizontal wind components, and z is the geometric height. $\mathrm{Ri} < 0.25$ was taken to indicate dynamic instability and $\mathrm{Ri} > 1$ to indicate stable stratification (Holtslag and Moeng, 1991; Gryning et al., 2007).

Because both the MYJ and BouLac PBL schemes predict TKE, the model-output variable TKE_PBL was used in the analysis. Ri was computed from the WRF output variables according to the equation above. PBLH was read directly from the

https://doi.org/10.5194/egusphere-2026-3392
Preprint. Discussion started: 24 August 2026

Table 2. Statistical evaluation metrics of the simulated 2 m air temperature for different model configurations: root mean square error (RMSE), mean absolute error (MAE), normalised mean bias (NMB), and Pearson correlation coefficient (R).

Cases	RMSE (°C)	MAE (°C)	NMB	R
MYJ & BEP & MODIS	2.83	2.37	−0.06	0.79
MYJ & BEP & LCZ	2.43	2.10	−0.05	0.81
MYJ & BEP–BEM & MODIS	2.05	1.61	−0.03	0.79
MYJ & BEP–BEM & LCZ	1.77	1.32	−0.01	0.80
BouLac & BEP–BEM & LCZ	1.53	1.06	0.00	0.84

model output and was cross-checked against the height of the TKE maximum to ensure a consistent description of the spatio-temporal evolution of the boundary-layer top. For the subsequent analysis, the model TKE was interpolated onto a non-uniform vertical grid spanning 0–2500 m. Specifically, the interpolation interval was 5 m within 10–50 m, 10 m within 50–200 m, 20 m within 200–500 m, 50 m within 500–1000 m, 100 m within 1000–2000 m, and 200 m within 2000–2500 m, expanding the vertical resolution from 40 to 71 levels and providing a more refined representation of the turbulent vertical structure from the surface layer to the boundary-layer top. Spatial averages were then computed separately for the CUR, the rural reference area, and the LCZ 1, 2, 4, 6, and 8 samples. On this basis, temporal composites (means) were constructed for the NHW and HW periods to compare the air temperature, UHII, TKE, and Ri characteristics between the two regimes.

3 Results

3.1 Model evaluation

The performance of the BEP and BEP–BEM urban canopy schemes, the MODIS and LCZ land-cover datasets, and the MYJ and BouLac PBL schemes was compared in this study. The 2 m air temperature was evaluated over the entire D03 domain against 73 AWSs; the harmonised PBLH dataset was used to evaluate PBLH over both the rural reference area and the CUR; and the Qingyuan IGRA soundings were used to evaluate the regional vertical profiles of temperature and wind. The statistics summarised in Table 2 showed that BEP–BEM produced 2 m air temperatures closer to the observations than BEP, and that replacing the default land cover with the LCZ dataset further improved the simulated 2 m air temperature. The BouLac scheme also outperformed MYJ in simulating PBLH (see Fig. S1 in the Supplement). Overall, the combination of BouLac, BEP–BEM, and LCZ provided the best performance, which is consistent with the configuration adopted by Li et al. (2026) over the same region.

We further evaluated this configuration over the CUR, the rural reference area, and in terms of CUHII. To ensure that the NHW and HW periods were comparable in sample length and simulation reliability, 6–8 July (3 days) was selected as the NHW period and the three hottest days of the first HW event (13–15 July, 3 days) were used for the HW analysis. Supplementary

https://doi.org/10.5194/egusphere-2026-3392
Preprint. Discussion started: 24 August 2026

results for the HW2 period (24–26 July) are provided in Figs. S7–S19 and Table S1. Fig. 3a–b showed that the simulated nighttime 2 m air temperature was biased high over the CUR during the NHW period, whereas the simulated daytime maximum was biased low over the rural area during the HW period. These two biases together produced the slight overall overestimation of the simulated CUHII over the CUR shown in Fig. 3c. The model captured the nighttime enhancement signal of ΔCUHII but slightly overestimated the daytime signal (see Fig. S2). The diurnal phase of CUHII agreed well with the observations, and the model reproduced the multi-day UHII oscillation. The simulated background state and diurnal cycle of the CUHII over the CUR were therefore considered reliable. The PBLH evaluation over the rural area (Fig. 3d) indicated that nighttime and early-morning PBLH values tended to be underestimated (the troughs of the blue curve were typically lower than those of the black curve), while some afternoon peaks were slightly overestimated. Over the CUR (Fig. 3e), the simulated PBLH was higher than the harmonised product by approximately 343 m on average (about 42 %). It indicates uncertainty in the absolute simulated urban PBLH and in the precise upper extent of daytime urban mixing. For the BUHII definition, however, the rural PBLH was the lower of the urban and rural values at 98.7 % of the evaluated times and at all nighttime time steps, so the common dynamic upper limit H_c was almost always set by the comparatively well-reproduced rural PBLH. The positive urban PBLH bias therefore has little direct effect on the BUHII integration depth and the simulated PBLH was suitable for use as the integration upper limit of BUHII, although absolute urban PBLH heights and the precise upper boundary of daytime vertical transport should be interpreted cautiously.

The Qingyuan sounding comparison provided an independent evaluation of the simulated regional vertical structure (Fig. S20 and Tables S2 and S3). Across all matched levels at pressures ≥50 hPa, temperature had a bias of +0.07 °C and an RMSE of 1.46 °C, while wind speed had a bias of +0.87 m s^{-1} and an RMSE of 3.39 m s^{-1}; the circular MAE of wind direction was 29.8° (Table S2). Within the 1000–850 hPa layer, the temperature and wind speed RMSEs were 1.37 °C and 2.56 m s^{-1}, respectively, and the circular wind direction MAE was 28.4° (Table S3). The model therefore reproduced the background temperature structure and broad wind-direction pattern, although the larger wind-speed errors between 850 and 700 hPa warrant caution. Because the sounding site is outside the urban core, this evaluation supports the regional background and PBL-process representation but does not replace the urban AWS and PBLH evaluations.

The evaluation of CUHII and ΔCUHII for the individual LCZs (Fig. 4) showed that the simulations captured the diurnal cycle of CUHII across LCZs and the HW-induced amplification, with the compact zones (LCZ 1 and LCZ 2) exhibiting stronger CUHII and the open or low-rise zones (LCZ 6 and LCZ 8) exhibiting weaker CUHII, in agreement with the observations. Some discrepancies remained in the absolute magnitude and the daytime response (which was generally too strong). For example, the nighttime enhancement (positive ΔCUHII) of LCZ 1 and LCZ 2 was well captured, but their daytime ΔCUHII were overestimated. The simulated ΔCUHII curve of LCZ 4 most closely matched the observed shape. Despite a slight overestimation of the CUHII magnitude and of the daytime HW response, the model reliably reproduced CUHII, its inter-LCZ relative structure, and the nighttime-enhancement mechanism.

https://doi.org/10.5194/egusphere-2026-3392
Preprint. Discussion started: 24 August 2026

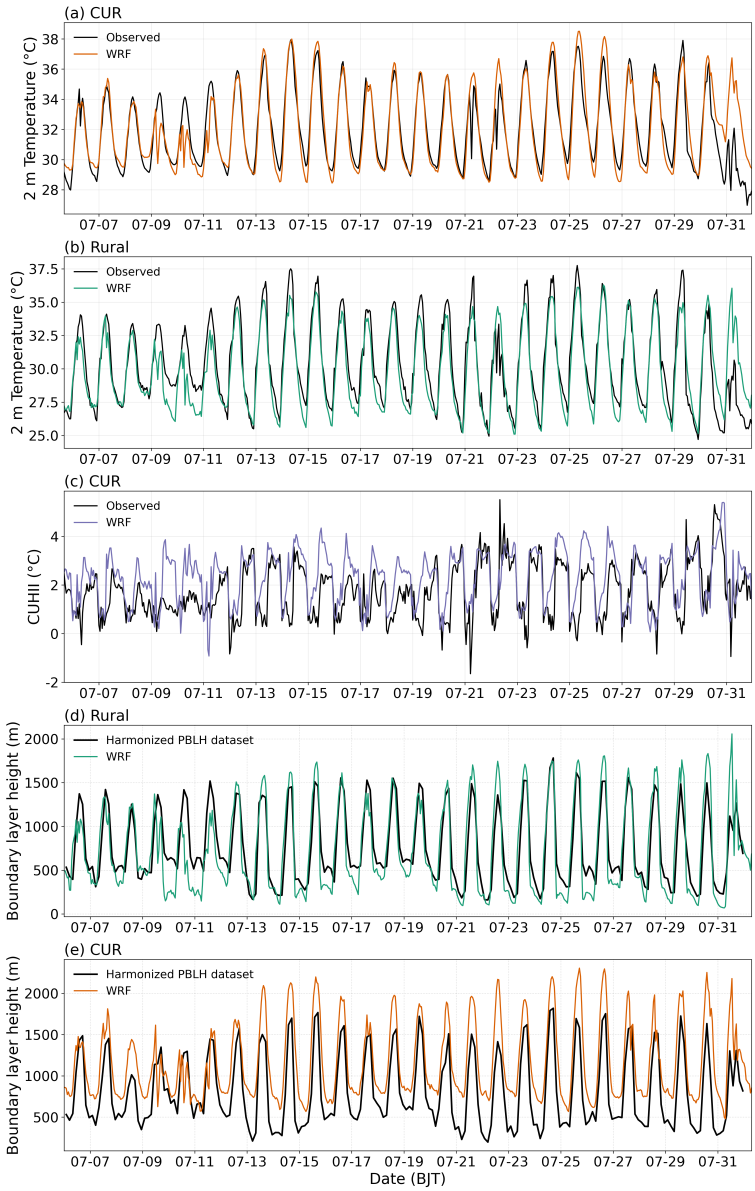

Figure 3. Comparison between simulations and observations during 6–31 July 2020 for (a) the 2 m air temperature over the CUR, (b) the 2 m air temperature over the rural reference area, and (c) the CUHII over the CUR. Simulated planetary boundary layer height (PBLH) over (d) the rural reference area and (e) the CUR compared with the harmonised PBLH dataset of Guo et al. (2022).

3.2 Vertical structure of urban thermal anomalies and HW-induced amplification

310 Figure 5 presented the vertical structure of air temperature and the urban–rural air temperature difference (ΔT) over the CUR and the rural area during the NHW and HW periods, providing an overall view of the vertical temperature field. During the

https://doi.org/10.5194/egusphere-2026-3392
Preprint. Discussion started: 24 August 2026

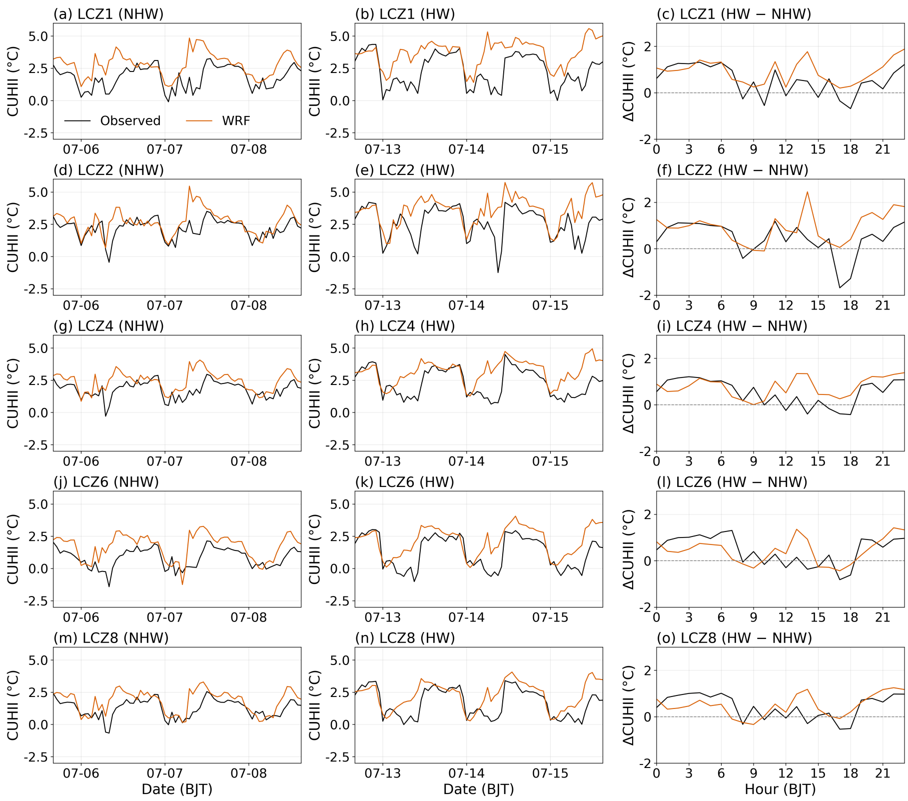

Figure 4. Comparison of simulated and observed CUHII and ΔCUHII for the individual LCZs. The left and middle columns show the CUHII during the NHW and HW periods, respectively, and the right column shows the diurnal cycle of ΔCUHII (HW - NHW) averaged over each period.

NHW period, the simulated positive ΔT layer extended upward to about 1000 m as the simulated PBL deepened, with a peak ΔT persisting between 15:00 and 20:00 BJT in the 300–400 m layer and below, while the 500–750 m layer remained relatively warm at night (Fig. 5c). During the HW period, the simulated positive ΔT layer extended higher, reaching as high as ∼1500 m in the early afternoon as the simulated PBL deepened (Fig. 5f); at night, the positive ΔT layer contracted and turned slightly negative above 500 m.

Figure 6 further showed the CUHII, BUHII, and Layer ΔT curves for the CUR relative to the rural reference, representing the canopy UHII, the boundary-layer UHII, and the temperature differences across the individual layers, respectively. Daytime was defined as 07:00–18:00 BJT (when $Q^* > 0$) and nighttime as 19:00–06:00 BJT, so that the two periods partition the diurnal cycle into two 12 h windows. The morning (06:00–08:00 BJT) and evening (17:00–19:00 BJT) transition periods were defined as process-oriented windows straddling the day–night boundaries; they intentionally overlap the adjacent daytime and nighttime periods and are used only for interpreting transition dynamics, not as mutually exclusive averaging periods. As shown in Fig. 6a, the CUHII over the CUR was generally higher during the HW than during the NHW period, with the most

https://doi.org/10.5194/egusphere-2026-3392
Preprint. Discussion started: 24 August 2026

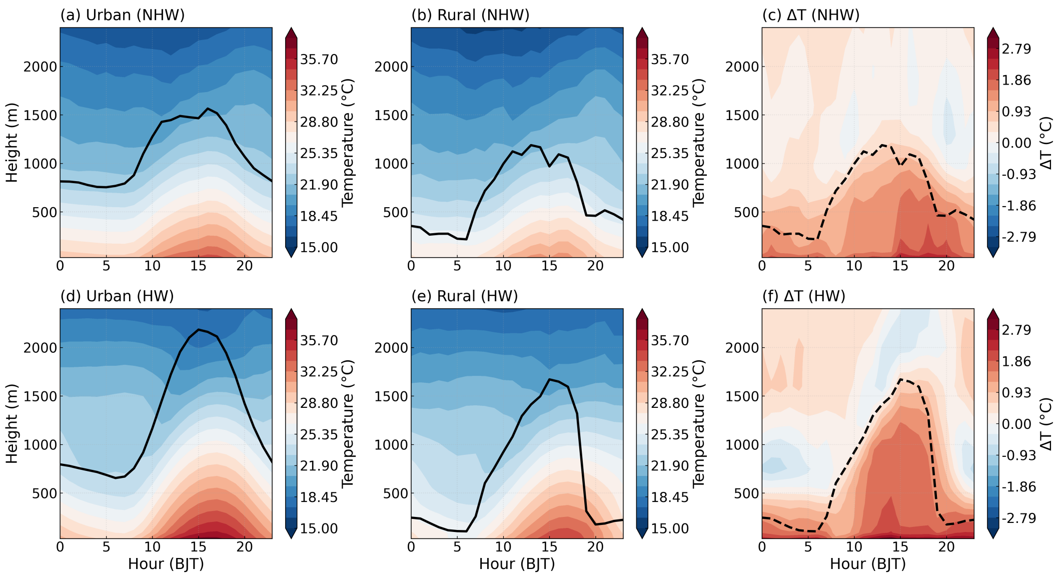

Figure 5. Vertical distributions of air temperature and the urban–rural air-temperature difference (ΔT) within 2500 m above ground over the urban and rural areas during the NHW and HW periods. The black solid lines in (a) and (d) indicate the urban PBLH; the black solid lines in (b) and (e) indicate the rural PBLH; the black dashed lines in (c) and (f) indicate the common dynamic PBL top used for the integration of BUHII during the NHW and HW periods.

pronounced enhancement occurring at night and in the early evening. BUHII was also enhanced under HW conditions, but with a smaller increase and a smoother diurnal evolution than CUHII. The Layer ΔT over the CUR provided a more direct view of the vertical transfer of HW-induced warming. Under NHW conditions, CUHII remained positive throughout the day, and ΔT in the 30–100 m, 100–250 m, 250–500 m, and 500–1000 m layers was also generally positive, with magnitudes decreasing with height (Fig. 6b). During the HW period, ΔT in each layer changed to varying degrees. Figure 6d showed that $\Delta\Delta T$ was generally positive from late morning to early afternoon (during the daytime period, especially 11:00–15:00 BJT), reflecting a clear daytime amplification. From midnight to early morning (00:00–06:00 BJT), $\Delta\Delta T$ remained positive at 2 m (i.e. CUHII), 30–100 m, and 100–250 m. The HW2 supplementary analysis (Fig. S8d) showed that $\Delta\Delta T$ in these layers exhibited a slight decreasing tendency but remained positive. Similarly, from early evening into the late night (19:00–23:00 BJT), $\Delta\Delta T$ increased again at 2 m, with somewhat weaker enhancement in the 30–100 m and 100–250 m layers. This indicated that the urban–rural ΔT below 250 m was amplified at night during the HW. In contrast, $\Delta\Delta T$ above 250 m gradually weakened after the early evening and approached zero or even became negative at night, indicating that the HW-induced amplification of the urban–rural ΔT did not propagate effectively to the mid-to-upper layers; that is, the upward transfer of the additional warming exhibited a disruption.

It is worth noting that the changes in ΔT across layers were not synchronous during the transition periods. Figure 6c showed that during the evening transition of the HW period (17:00–19:00 BJT), ΔT at 2 m rose markedly, while the 30–250 m layers

https://doi.org/10.5194/egusphere-2026-3392
Preprint. Discussion started: 24 August 2026

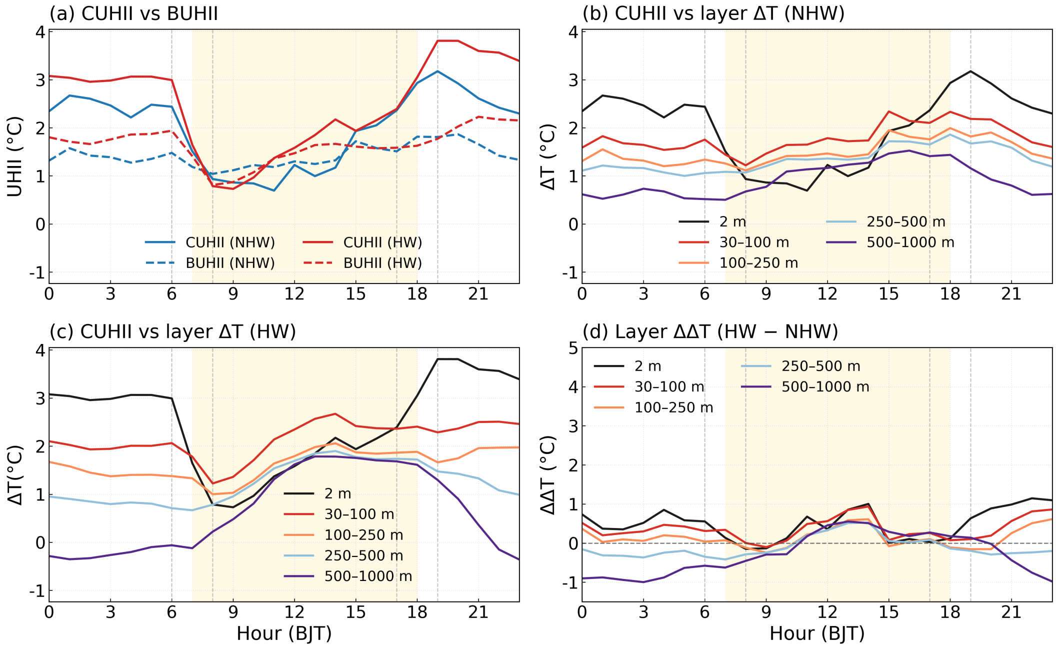

Figure 6. Diurnal cycles over the CUR. (a) CUHII (solid) and BUHII (dashed) during the NHW (blue) and HW (red) periods. (b) Layer ΔT at 2 m, 30–100 m, 100–250 m, 250–500 m, and 500–1000 m during the NHW period. (c) Same as (b) but for the HW period. (d) $\Delta\Delta T$ (HW - NHW) at the same five layers. Light-yellow shading indicates the daytime period (07:00–18:00 BJT); the hatched periods 06:00–08:00 BJT and 17:00–19:00 BJT indicate the morning and evening transitions, respectively.

changed little during this period and only increased slowly after 18:00 BJT, exhibiting a response lag relative to the surface. The 250–500 m layer showed a slight decreasing tendency but remained stable in the late night and the early hours of the following day. The decrease in the 500–1000 m layer was more pronounced. During the morning transition (06:00–08:00 BJT), ΔT below 250 m generally weakened rapidly, whereas the layers above 250 m largely remained stable or even slightly increased. Together, these features indicated that, in the transition periods, the evening was characterised by an early recovery of warming in the lower layers and a decay aloft, whereas the morning was characterised by decay in the lower layers and persistence (or even a slight strengthening) aloft. This suggested that nocturnal residual-layer warm anomalies in the city were entrained into the developing mixed layer the following morning, thereby maintaining a positive ΔT in the middle layers. Figure 6c–d further indicated that the morning persistence (and even slight strengthening) of upper-level ΔT was more pronounced under HW than under NHW conditions, suggesting that the HW enhanced this "memory" effect of the residual layer.

3.3 LCZ-dependent vertical response and residual-layer thermal memory

Figure 7 showed the diurnal cycles of CUHII and BUHII for the individual LCZs during the NHW and HW periods, together with the HW-induced increments (ΔCUHII and ΔBUHII). During the NHW period, the inter-LCZ ranking of CUHII was

https://doi.org/10.5194/egusphere-2026-3392
Preprint. Discussion started: 24 August 2026

relatively stable (Fig. 7a): LCZ 1 was consistently the strongest; LCZ 4 and LCZ 2 lay at intermediate-to-high levels; LCZ 8 and LCZ 6 were relatively weak; and LCZ 6 was the lowest at most times. By contrast, BUHII had a markedly smaller diurnal amplitude than CUHII, with smoother curves and substantially reduced inter-LCZ differences (Fig. 7b). This indicated that the LCZ-induced heterogeneity of UHII was concentrated in the canopy and the lower part of the boundary layer and was appreciably damped once the boundary-layer-mean was taken. During the HW period, CUHII was enhanced for every LCZ relative to the NHW period (Fig. 7c–e). The increase in ΔCUHII for LCZ 1 was the most pronounced, with a daily mean of 0.77 °C (Table 3); LCZ 4 and LCZ 2 also showed consistently positive but slightly weaker increments of 0.64 and 0.58 °C, respectively. LCZ 6 and LCZ 8 exhibited the weakest enhancement, at 0.38 and 0.46 °C, respectively. Compared with CUHII, the inter-LCZ spread of BUHII during the HW period remained small, although it was slightly larger than during the NHW period.

To examine the vertical response of the individual LCZs during the HW in more detail, layer-mean temperature differences (Layer ΔT) between each LCZ and the rural reference area were computed (see Fig. S4). The Layer ΔT of the different LCZs exhibited clear near-surface heterogeneity: LCZ 1 and LCZ 4 had generally stronger Layer ΔT, LCZ 2 lay in the middle, and LCZ 6 and LCZ 8 were relatively weak.

The HW-induced increment of Layer ΔT ($\Delta\Delta T$ = HW - NHW) was then computed to compare the vertical response of HW-induced additional warming across LCZs. Figure 8a–e showed that LCZ 1 exhibited the strongest low-level (below 250 m) $\Delta\Delta T$ during most periods of the day (00:00–08:00, 11:00–15:00, and 21:00–23:00 BJT). The low-level $\Delta\Delta T$ of LCZ 4 was slightly weaker than that of LCZ 1 but was more coherent during the daytime, whereas LCZ 2 was slightly stronger than LCZ 4 at night. LCZ 6 was the weakest, with the additional warming extending up to 250 m only in the early afternoon and at night, while a clear disruption of the vertical transfer from the lower layers to higher layers occurred during the morning and evening transitions. Taking the 30–100 m layer as an example (Table 3), the daily mean $\Delta\Delta T$ of LCZ 1 reached 0.54 °C, with daytime and nighttime values of 0.56 and 0.52 °C, respectively. LCZ 4 and LCZ 2 reached daily mean $\Delta\Delta T$ of 0.47 and 0.43 °C, with daytime values of 0.45 and 0.36 °C and nearly equal nighttime values (or a slightly stronger LCZ 2 in HW2; see Table S1). LCZ 6 had a daily mean $\Delta\Delta T$ of only 0.28 °C.

To place the additional warming of these LCZs within the urban context, the Layer $\Delta\Delta T$ of each LCZ was differenced against the CUR-mean Layer $\Delta\Delta T$ to obtain its deviation pattern from the urban mean. Because LCZ 8 contained a large fraction of the samples within the CUR and was closest to the urban-mean state, it was treated as the background type. As shown in Fig. 8f–j, LCZ 1 exhibited a stronger positive deviation from the CUR mean below 500 m during most of the day (00:00–16:00 BJT), together with a more pronounced negative deviation in the evening and at night—particularly the column-wide negative deviation between 19:00 and 21:00 BJT. This indicated that the additional warming of LCZ 1 decayed faster than the CUR mean during the transition periods, with a larger diurnal amplitude and a more sensitive response. The deviation patterns of LCZ 4 and LCZ 2 were broadly similar, with weaker positive and negative deviations than LCZ 1; the early-afternoon mid- to low-level positive deviation of LCZ 4 was slightly stronger than that of LCZ 2. LCZ 6 showed mostly negative or near-zero deviations from the CUR mean throughout most of the day, particularly in the lower layers, with only

https://doi.org/10.5194/egusphere-2026-3392
Preprint. Discussion started: 24 August 2026

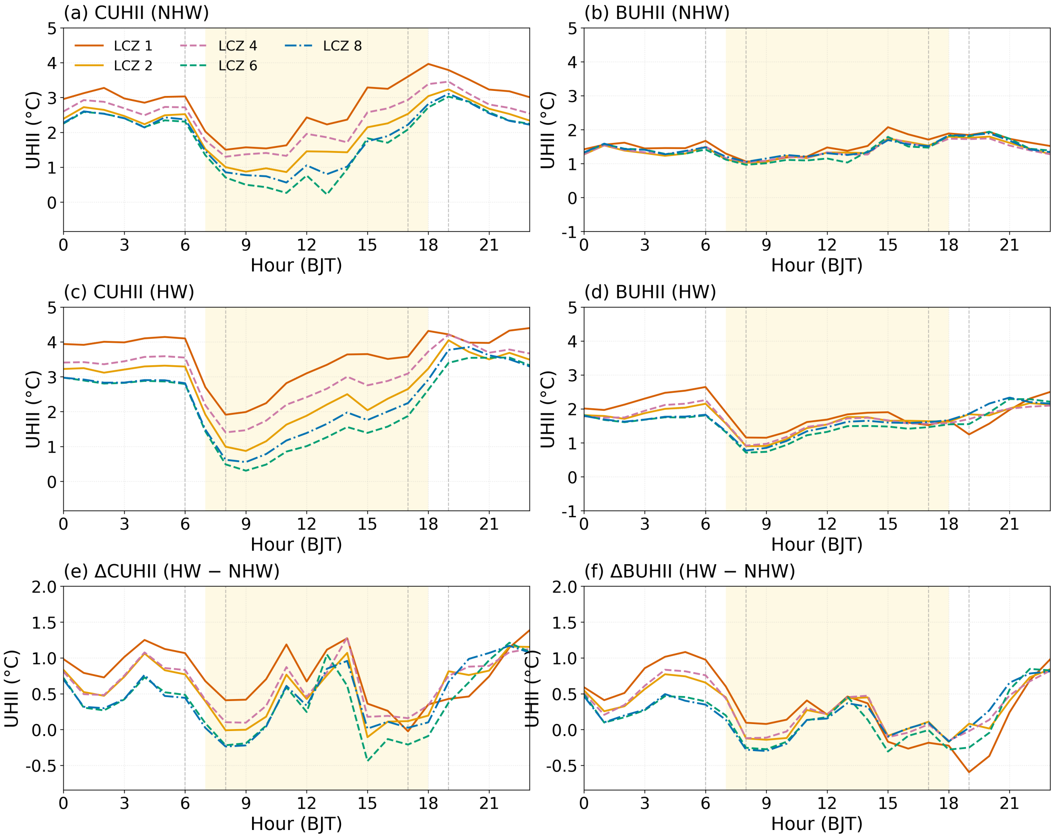

Figure 7. CUHII and BUHII diurnal cycles for the individual LCZs during the NHW and HW periods. (a) CUHII during the NHW period; (b) BUHII during the NHW period; (c) CUHII during the HW period; (d) BUHII during the HW period; (e) ΔCUHII (HW - NHW); (f) ΔBUHII (HW - NHW). Light-yellow shading indicates the daytime period (07:00–18:00 BJT); the hatched periods 06:00–08:00 BJT and 17:00–19:00 BJT indicate the morning and evening transitions, respectively.

brief positive excursions at certain times, representing the weakest additional-warming response relative to the urban mean. LCZ 8 remained close to zero throughout the day, supporting its suitability as a background for the CUR.

Figure 8 revealed the differentiated vertical distribution of HW-induced additional warming among LCZs. To further examine whether the thermal-memory effect noted in Sect. 3.2 was modulated by LCZ, Fig. 9 showed the diurnal ΔT evolution at the 500–600 m layer alone—located within the lower portion of the typical nocturnal residual-layer band (∼500–1500 m) for this subtropical-high regime (see Fig. S6 for the layer-selection diagnostic)—for inter-LCZ comparison. During the NHW period, inter-LCZ differences in ΔT were small, and the LCZ dependence of the memory effect was weak. During the HW period (Fig. 9b), inter-LCZ differences became markedly larger. From night to early morning (00:00–06:00 BJT), LCZ 1 maintained the highest ΔT (up to 0.41 °C) without any clear decay, indicating that its residual-layer warm anomaly persisted until the following morning. LCZ 2 and LCZ 4 showed similar but somewhat weaker behaviour. The ΔT of LCZ 6 decreased towards

https://doi.org/10.5194/egusphere-2026-3392
Preprint. Discussion started: 24 August 2026

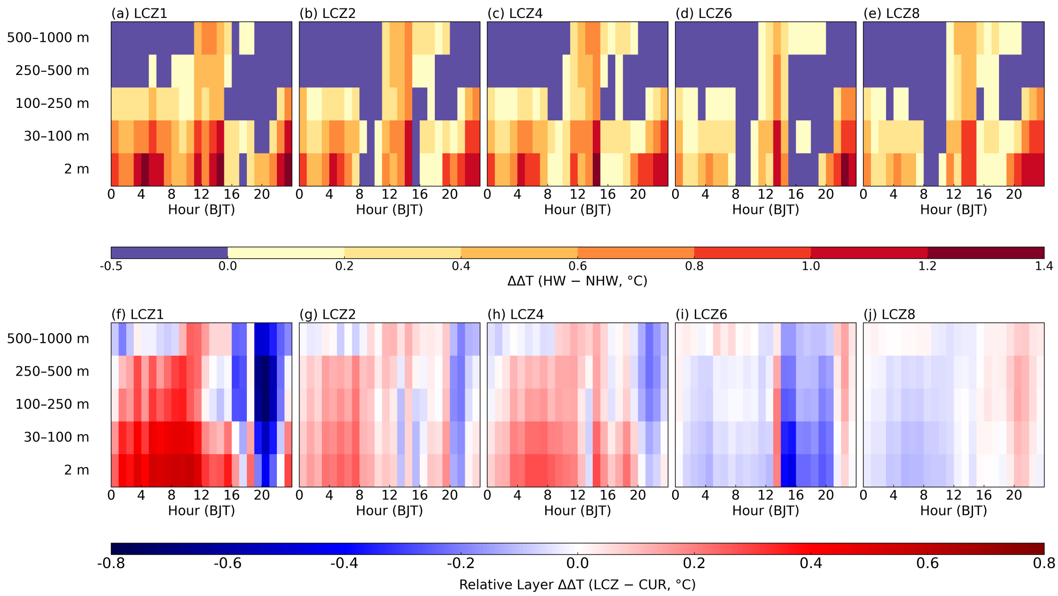

Figure 8. (a–e) Vertical distribution of Layer $\Delta\Delta T$ (HW - NHW) for LCZ 1, 2, 4, 6, and 8, respectively. (f–j) Deviations of each LCZ's Layer $\Delta\Delta T$ from the CUR-mean Layer $\Delta\Delta T$, in the same order as (a–e). Note that (a–e) and (f–j) use different colour scales.

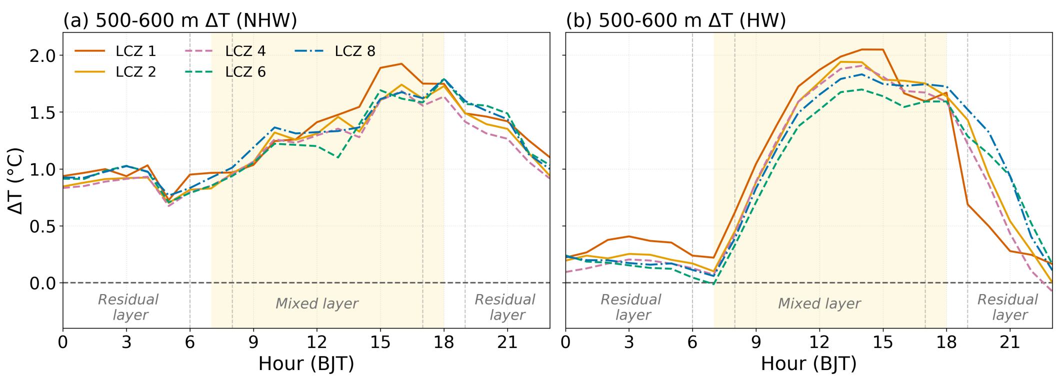

Figure 9. Diurnal cycles of ΔT at 500–600 m for individual LCZs during (a) the NHW period and (b) the HW period.

dawn, implying that the residual-layer warm anomaly was already substantially weakened before sunrise and that less heat was available for entrainment into the developing mixed layer the next day. During the morning transition (06:00–08:00 BJT), ΔT in all LCZs rose rapidly with the development of the mixed layer; LCZ 1 started from a higher level and reached the largest early-afternoon peak. Notably, LCZ 1 also showed a brief sharp drop in ΔT in the early evening (around 18:00 BJT), consistent with the high-amplitude response feature shown in Fig. 8f.

https://doi.org/10.5194/egusphere-2026-3392
Preprint. Discussion started: 24 August 2026

3.4 Surface energy partitioning, turbulence, and the LCZ modulation of vertical heat transfer

3.4.1 Surface energy balance and turbulence response over the urban–rural contrast

To explain these differences, Figs. 10 and 11 presented the diurnal cycles of the surface energy balance components over the CUR and the rural area during the NHW and HW periods, together with the HW-induced changes in turbulence kinetic energy (ΔTKE) and gradient Richardson number (ΔRi). Following our methodology, the Bowen ratio was computed only during daylight hours (when $Q^* > 0$) to avoid spurious values associated with very small nocturnal $Q_{\rm E}$. TKE and Ri were used to characterise the intensity of turbulent mixing and the static stability of the stratification, respectively. Figure 10e additionally showed the diurnal cycle of the residual-method $Q_{\rm F}$. Over the rural reference area, $Q_{\rm F}$ remained close to zero throughout the day (daily mean < 5 W m^{-2}), indicating that the BEP–BEM scheme achieved a good energy closure over natural surfaces. Over the urban area, $Q_{\rm F}$ displayed the typical signature of BEM building waste-heat: an early-morning minimum (30–50 W m^{-2}) and an afternoon-to-evening peak ($\sim$85 W m^{-2} during the NHW period and $\sim$105 W m^{-2} during the HW period), of comparable magnitude to existing anthropogenic-heat estimates in the Greater Bay Area (Cao et al., 2019). $Q_{\rm F}$ increased by approximately 17 % at all hours during the HW relative to the NHW, reflecting the response of air-conditioning loads to ambient temperature. The near-zero rural baseline further supported the interpretation of the non-zero urban $Q_{\rm F}$ signal as a genuine contribution from unresolved building physical processes rather than a numerical residual.

The surface energy balance (Fig. 10) showed that daytime Q^* was markedly enhanced over both the CUR and the rural area during the HW (Fig. 10a), and that the rural peak was not lower than that of the CUR during certain periods, indicating that both surface types received strong radiative input under HW conditions. However, $Q_{\rm H}$ over the CUR was clearly enhanced during the HW and was sustained at high levels from late morning into the afternoon (Fig. 10b). By contrast, the rural area partitioned a larger fraction of available energy into $Q_{\rm E}$, with daytime $Q_{\rm E}$ far exceeding that of the CUR (Fig. 10c). Correspondingly, the daytime Bowen ratio over the CUR was substantially higher than that over the rural area, and was further increased under HW conditions, while the rural area maintained a consistently low Bowen ratio (Fig. 10f). This implied that, under HW conditions, the CUR preferentially converted available energy directly into sensible heat, whereas the rural area favoured latent heat, in agreement with previous urban–rural energy-partitioning studies during HWs (Li and Bou-Zeid, 2013; Sun et al., 2017; Kong et al., 2021). The ground heat flux $Q_{\rm G}$ during daytime over the CUR became more strongly negative under HW conditions, indicating enhanced downward heat transfer into the substrate. In the evening and at night, $Q_{\rm G}$ over the CUR turned more positive than during the NHW period, as the heat accumulated during the day was released back to the atmosphere. At the same time, the anthropogenic heat flux $Q_{\rm F}$ over the CUR persisted throughout the day and was further enhanced during the HW, while $Q_{\rm F}$ over the rural area remained close to zero (Fig. 10e).

This contrast in surface energy partitioning was further modulated by stability and turbulence adjustments. Relative to the NHW period, daytime ΔRi over the CUR was markedly reduced from the surface layer up into the lower boundary layer (Fig. 11d), with persistently negative values (red shading) particularly in the 100–300 m layer; similar changes occurred over the rural area (Fig. 11e), indicating that the lower-to-middle layers became substantially more unstable during the HW. During the HW, positive ΔTKE (HW - NHW) over the CUR mainly appeared at simulated heights of about 500–1400 m in the early

https://doi.org/10.5194/egusphere-2026-3392
Preprint. Discussion started: 24 August 2026

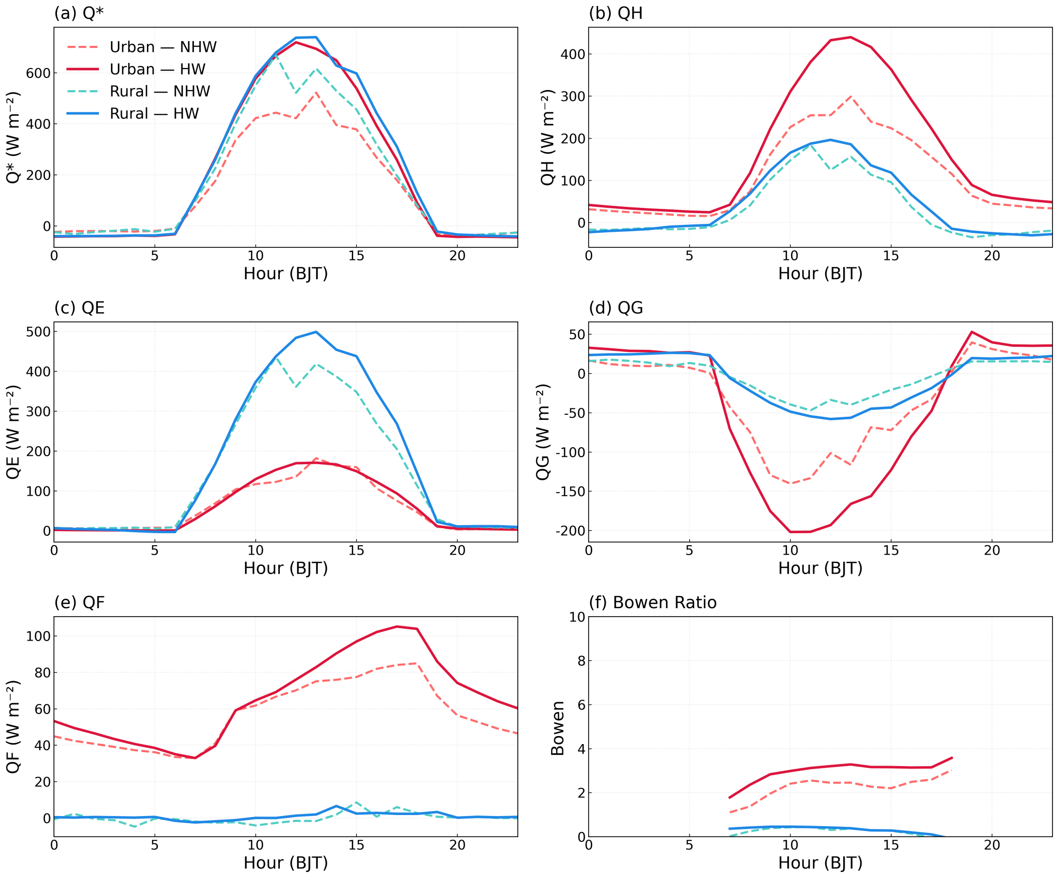

Figure 10. Diurnal cycles of the components of the surface energy-balance over urban (red) and rural (blue) areas during the NHW (dashed) and HW (solid) periods: (a) net radiation Q^*; (b) sensible heat flux Q_{H}; (c) latent heat flux Q_{E}; (d) ground heat flux Q_{G}; (e) anthropogenic heat flux Q_{F} (estimated as a residual); and (f) Bowen ratio, calculated only when $Q^* > 0$.

afternoon (Fig. 11a). Although positive ΔTKE also occurred over the rural area, both its intensity and its vertical coherence were markedly weaker (Fig. 11b). The CUR–rural differences ΔΔTKE (defined as the CUR–rural difference of ΔTKE) and ΔΔRi were then computed; ΔΔRi exhibited no clear vertical-temporal pattern, whereas positive ΔΔTKE was mainly confined to the mid-to-upper part of the daytime developing boundary layer, with the near-surface layer generally showing weaker or even slightly negative ΔΔTKE (Fig. 11c). This indicated that, relative to the rural area, the stronger sensible heat input and lower stability over the CUR under HW conditions did not translate into a uniform synchronous enhancement of near-surface turbulence; rather, they manifested as enhanced turbulent activity in the mid-to-upper layers and an upward shift of its centre. Such a configuration favoured upward transport of additional surface heat, and, because this effect was stronger over the urban than over the rural area (Fig. 11c), it promoted the upward extension of HW-induced additional warming during the daytime.

https://doi.org/10.5194/egusphere-2026-3392
Preprint. Discussion started: 24 August 2026

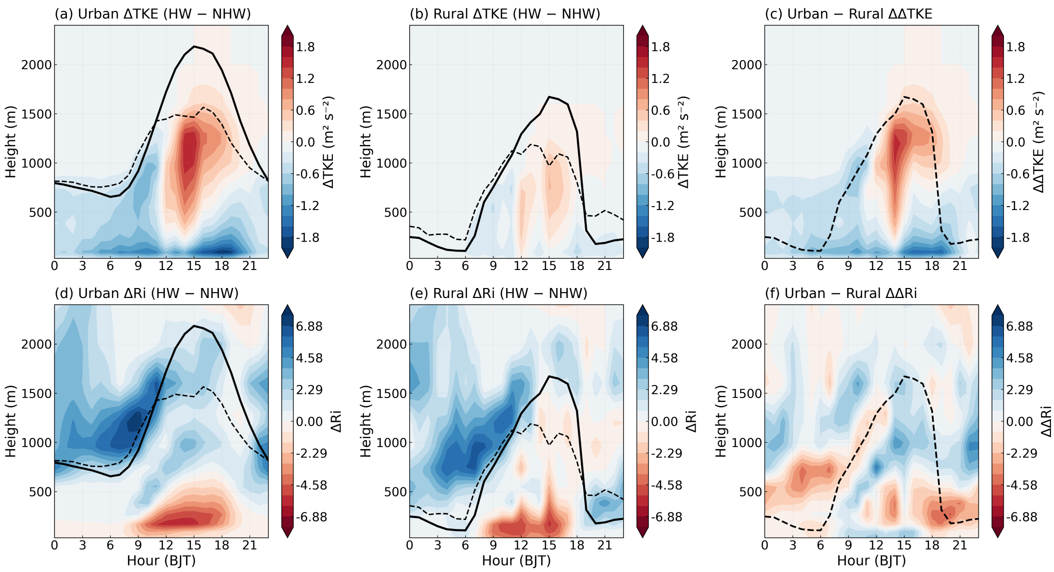

Figure 11. Vertical distributions of ΔTKE (HW - NHW; top row) and ΔRi (HW - NHW; bottom row): (a, d) over the urban area; (b, e) over the rural reference area; and (c, f) the urban–rural difference (ΔΔTKE and ΔΔRi). The black solid and dashed lines in (a) and (d) denote the urban PBLH during the HW and NHW periods, respectively; those in (b) and (e) denote the rural PBLH during the HW and NHW periods, respectively; and the black dashed lines in (c) and (f) denote the common dynamic PBL top H_c(t) during the HW period.

At night, the enhanced Q_G combined with the weaker low-level turbulence (Fig. 11a) favoured the accumulation of heat near the surface, sustaining persistently positive $\Delta\Delta T$ below 250 m at night.

3.4.2 LCZ-dependent surface energy partitioning and turbulence pathways

Figures 12 and 13 summarise the LCZ-dependent HW–NHW responses in surface energy partitioning and turbulence: Fig. 12 shows the HW-induced changes in key surface-energy indicators, while Fig. 13 shows the deviations of the LCZ-scale turbulence response from the CUR-mean response. Figure 12 showed that daytime Q_H was enhanced under HW conditions for every LCZ, and that nocturnal $\Delta(Q_G + Q_F)$ was also generally increased under HW conditions; however, the energy partitioning differed substantially among LCZs. LCZ 1 had the largest daytime Q_H enhancement ($\Delta Q_H \approx$ 120.1 W m^{-2}; Table 3), the largest Q_E reduction ($\Delta Q_E \approx$ -19.5 W m^{-2}), the highest ΔBowen (∼3.5), and the strongest combined nocturnal heat-storage release and anthropogenic heat ($\Delta(Q_G + Q_F) \approx$ 43.7 W m^{-2}). These features were consistent with the high building density and large impervious-surface fraction of LCZ 1. LCZ 2 also showed strong ΔQ_H (102.3 W m^{-2}), high ΔBowen, and pronounced nocturnal heat-storage release and anthropogenic heat, in line with its compact midrise morphology. By contrast, LCZ 4, an open high-rise zone with a slightly lower impervious-surface fraction, showed a ΔQ_H weaker than that of LCZ 2 and a slightly positive ΔQ_E, but its nocturnal $\Delta(Q_G + Q_F)$ remained substantially positive. LCZ 6 exhibited the weakest ΔQ_H (∼81.5 W m^{-2}), the largest positive ΔQ_E (∼26.7 W m^{-2}), the lowest ΔBowen (0.3), and the smallest nocturnal heat-storage

https://doi.org/10.5194/egusphere-2026-3392
Preprint. Discussion started: 24 August 2026

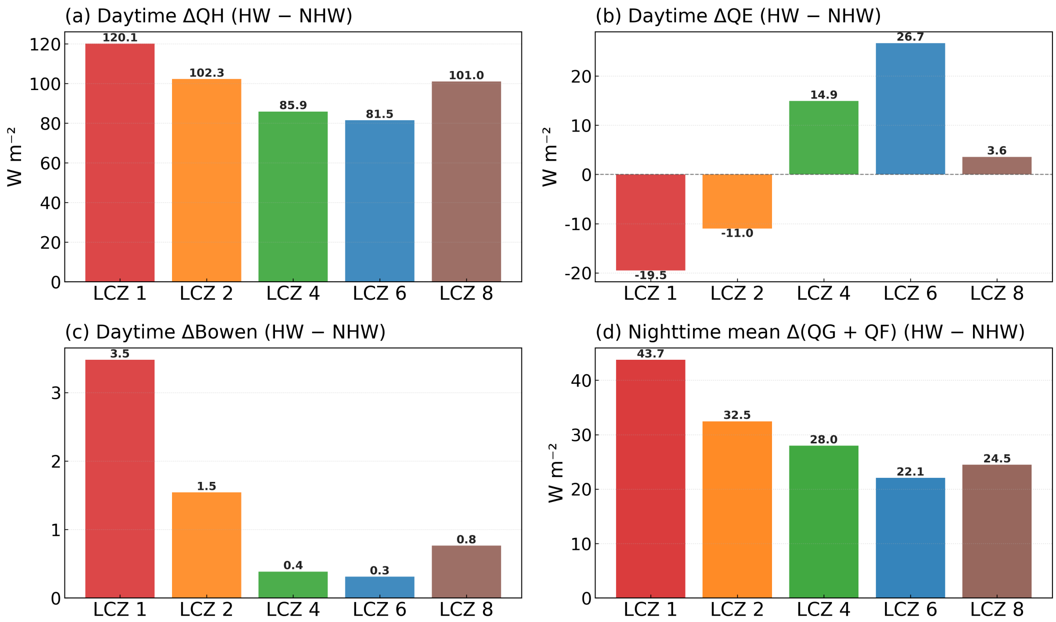

Figure 12. HW - NHW differences in surface energy-balance indicators for the individual LCZs: (a) daytime mean ΔQ_{H}; (b) daytime mean ΔQ_{E}; (c) daytime mean ΔBowen ratio; and (d) mean nocturnal $\Delta(Q_{\mathrm{G}} + Q_{\mathrm{F}})$. The numerical values are annotated on each bar.

release and anthropogenic heat ($\Delta(Q_{\mathrm{G}} + Q_{\mathrm{F}}) \approx 22.1$ W m^{-2}), consistent with its open low-rise morphology and relatively small impervious-surface fraction.

The deviations of each LCZ from the CUR mean in the surface-energy response terms (ΔQ_{H}, ΔQ_{E}, ΔBowen, and $\Delta(Q_{\mathrm{G}} + Q_{\mathrm{F}})$; Fig. S5) and in the turbulence response (ΔΔTKE; Fig. 13) provided a complementary view. Here, ΔΔTKE denotes the deviation of each LCZ's HW–NHW TKE response from the CUR-mean response; because the same rural ΔTKE is subtracted when forming the relative urban–rural contrast, this quantity is numerically equivalent to the LCZ–CUR deviation in ΔTKE. Relative to the NHW period, LCZ 1 exhibited a large diurnal $\Delta\Delta T$ amplitude (Fig. 8f) and a sensitive ΔΔTKE response (Fig. 13a): in the simulation, positive ΔΔTKE was mainly found between 1000 and 1900 m in the early afternoon, with the maximum at about 1600 m, and a clear sign reversal occurred around 17:00–18:00 BJT. The pattern for LCZ 2 was similar to that of LCZ 1, but weaker (Fig. 13b). LCZ 4 had a weaker additional sensible-heat input than LCZ 2, but its positive ΔΔTKE in the mid-to-low layers below 500 m was stronger and more coherent than LCZ 2, with positive deviations particularly easy to maintain in the 100–500 m layer in the afternoon (Fig. 13c). LCZ 6 showed negative deviations in sensible heat, Bowen ratio, and nocturnal heat sources relative to the CUR, and its ΔΔTKE was also generally weaker, especially in the afternoon when the entire column was weaker than the CUR mean (Fig. 13d).

To further quantify the differences in the energy–turbulence–thermal-response relationship among LCZs, Fig. 14 presented the scatter relationship between daytime ΔQ_{H} and the daily mean $\Delta\Delta T$ in the 30–100 m layer, and that between the daytime mean ΔΔTKE below 250 m and $\Delta\Delta T$. ΔQ_{H} and $\Delta\Delta T$ tracked each other across the compact and low-rise LCZs (1, 2, 6,

https://doi.org/10.5194/egusphere-2026-3392
Preprint. Discussion started: 24 August 2026

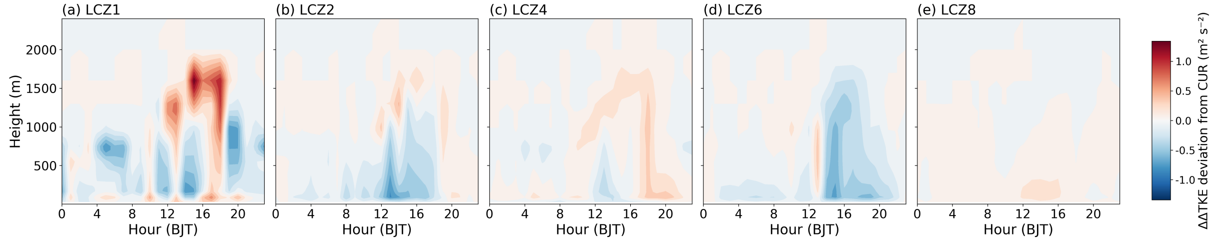

Figure 13. Vertical distributions of ΔΔTKE, defined here as the deviation of each LCZ's HW–NHW TKE response from the CUR-mean response, for (a) LCZ 1, (b) LCZ 2, (c) LCZ 4, (d) LCZ 6, and (e) LCZ 8.

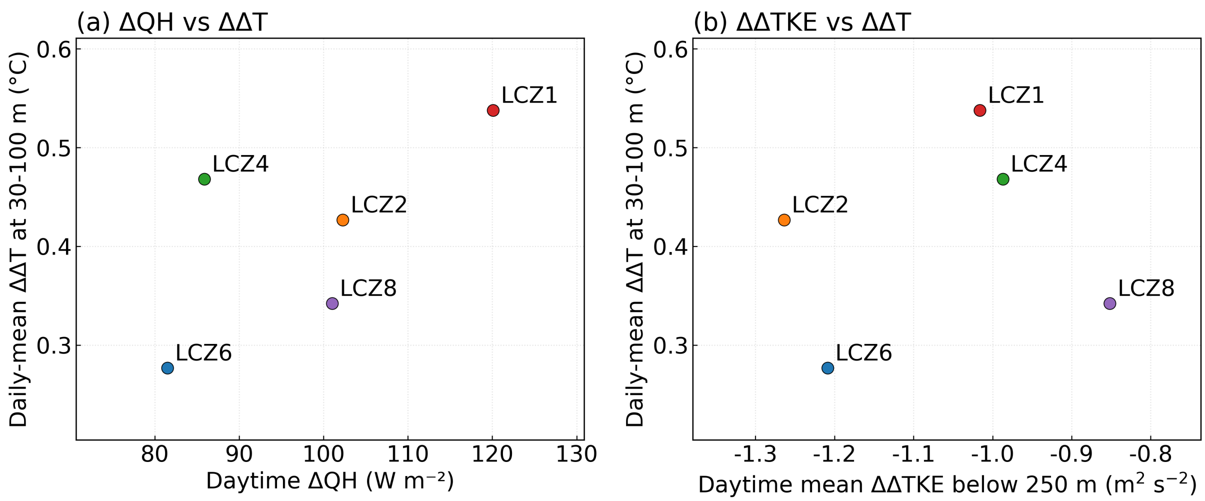

Figure 14. Scatter plots of the daily mean $\Delta\Delta T$ in the 30–100 m layer for individual LCZs against (a) the daytime mean ΔQ_{H}, and (b) the daytime mean ΔΔTKE below 250 m.

8): higher daytime sensible-heat enhancement aligned with stronger 30–100 m additional warming. LCZ 4 departed from this alignment: its ΔQ_{H} (85.9 W m^{-2}) was close to LCZ 6's (81.5 W m^{-2}), yet its $\Delta\Delta T$ (0.47 °C) was close to LCZ 2's (0.43 °C). Figure 14b explained this departure: the magnitude of the negative ΔΔTKE of LCZ 4 was markedly smaller than those of LCZ 2 and LCZ 6, indicating that the low-level turbulence damping under HW conditions was comparatively weaker over LCZ 4. This favoured the maintenance of mid-to-low-level heat mixing and transport, which might compensate for the weaker additional sensible-heat input. By contrast, although LCZ 2 received a stronger sensible heat input, its turbulence damping relative to the CUR was also greater. Hence, LCZ 2 and LCZ 4 reached a comparable level of HW-induced additional warming in the 30–100 m layer through different energy–turbulence pathways.

Overall, the HW expanded the daytime urban–rural ΔT upward, but this enhancement was vertically non-uniform: the response was most robust in the 30–250 m layer; mid- to upper-level enhancement occurred primarily during the afternoon mixing-layer development; and the night and evening were characterised by coexisting near-surface intensification and a weak-

https://doi.org/10.5194/egusphere-2026-3392
Preprint. Discussion started: 24 August 2026

Table 3. Indicators of thermal response and surface energy-balance response of the individual LCZs during the HW compared to the NHW period. Δ denotes HW - NHW.

Indicator	LCZ 1	LCZ 2	LCZ 4	LCZ 6	LCZ 8
ΔCUHII daily mean (°C)	0.77	0.58	0.64	0.38	0.46
ΔCUHII nocturnal mean (°C)	0.93	0.83	0.84	0.65	0.70
30–100 m $\Delta\Delta T$ daily mean (°C)	0.54	0.43	0.47	0.28	0.34
30–100 m $\Delta\Delta T$ daytime mean (°C)	0.56	0.36	0.45	0.20	0.28
30–100 m $\Delta\Delta T$ nocturnal mean (°C)	0.52	0.49	0.49	0.35	0.40
ΔQ_{H} daytime mean ($\mathrm{W\,m^{-2}}$)	120.1	102.3	85.9	81.5	101.0
ΔQ_{E} daytime mean ($\mathrm{W\,m^{-2}}$)	−19.5	−11.0	14.9	26.7	3.6
ΔBowen daytime mean	3.5	1.5	0.4	0.3	0.8
$\Delta(Q_{\mathrm{G}}+Q_{\mathrm{F}})$ nocturnal mean ($\mathrm{W\,m^{-2}}$)	43.7	32.5	28.0	22.1	24.5

ened upper-level response. These thermal responses differed clearly among LCZs in the lower layers, indicating that the HW-induced amplification of UHII manifested not only as a magnitude increase but also as differentiated vertical responses of thermal anomalies under different urban morphologies. The vertical responses of individual LCZs under HW conditions were jointly modulated by differences in surface energy partitioning and in boundary-layer turbulence response. LCZ 1 had the strongest additional sensible heat input and the largest diurnal amplitude during most periods, dominating the low-level additional warming response. LCZ 2 and LCZ 4 lay at intermediate levels with similar deviation patterns, reaching comparable additional warming through different energy–turbulence pathways, while LCZ 6, with both weak sensible heat and weak turbulence, exhibited the weakest and shallowest response. These differences in surface energy partitioning affected not only the vertical thermal response throughout the day, but also—through their influence on the residual-layer thermal-memory strength—the warming on the following day. As shown in Fig. 9 (Sect. 3.3), LCZ 1 maintained the strongest ΔT between 500 and 600 m at night during the HW, while the ΔT of LCZ 6 had already decreased substantially by early morning. This contrast was consistent with the inter-LCZ differences in nocturnal $\Delta(Q_{\mathrm{G}} + Q_{\mathrm{F}})$ (Table 3). It implied that the strongest nocturnal heat-source supply of LCZ 1, together with its taller building cluster and rougher surface, might weaken the decoupling between the near-surface layer and the residual layer, thereby sustaining a more persistent residual-layer warm anomaly. LCZ 6, by contrast, had the weakest nocturnal heat source, and its thermal-memory effect therefore decayed more rapidly. Supplementary analysis of the HW2 period (Fig. S12) showed that the same inter-LCZ ranking was reproduced, although with weaker absolute amplitude. LCZ 1 still retained the strongest residual-layer signal and LCZ 6 the weakest, with LCZ 1 exhibiting a slight downward tendency, consistent with the urban-mean trend in Fig. S8d. This might be related to the reduced rural evapotranspiration during the daytime (Fig. S13c) and the warmer rural near-surface air temperature at night (Fig. 3b) during the HW2 period, which together caused an overall convergence of the urban–rural ΔT in the morning.

https://doi.org/10.5194/egusphere-2026-3392
Preprint. Discussion started: 24 August 2026

4 Discussion

This study showed that the HW-induced amplification of UHII over the Guangzhou metropolitan area exhibited a pronounced vertical non-uniformity: the strongest response was concentrated within the canopy layer and immediately above it, while the boundary-layer-mean response was comparatively weak. The HW amplified UHII in every LCZ, but the magnitude and depth of the vertical response showed a clear morphology dependence. Both the vertical non-uniformity and the LCZ dependence were corroborated by the HW2 results (Figs. S7–S19 and Table S1).

Overall, our results were consistent with previous studies on HW-induced UHI amplification and aligned with recent work emphasising that the boundary-layer thermal structure under HWs has distinct vertical features. Earlier studies showed that HW–UHI synergy was jointly controlled by the background climate, urban–rural energy partitioning, and ventilation conditions (Kong et al., 2021; Jiang et al., 2019; Park and Baik, 2026). Recent boundary-layer studies further indicated that this synergy was highly height-dependent and could not be diagnosed from near-surface temperatures alone. At the same time, a substantial body of LCZ-based literature demonstrated that urban morphology exerts strong control on canopy-level heat (Ngarambe et al., 2020; Zong et al., 2021; Tian et al., 2023; Li et al., 2026); however, most LCZ studies remained focused on surface or canopy UHI and on horizontal thermal contrasts, while analyses in the vertical direction were still relatively scarce. The HW simulation of Xin et al. (2024) for Shanghai also showed that both near-surface and boundary-layer UHIs were enhanced under HW conditions, with the intensity decreasing with height, in agreement with our findings. That study, however, reported no significant nocturnal UHI response to the HW, whereas our results for Guangzhou showed that BUHII was also enhanced at night, particularly over compact LCZs. Xin et al. (2024) attributed the rapid weakening of UHI in Shanghai to a wind-direction shift that produced cold advection over the urban area, whereas the Guangzhou metropolitan area was under subtropical-high control during the present HW, with a limited horizontal-advection influence on the surface energy budget. This contrast suggested that synoptic regime and coastal circulation might modulate the nocturnal BUHII response during HWs, a hypothesis warranting testing on a larger sample of HW events spanning different background regimes. The atmospheric-boundary-layer (ABL) heat-budget analysis of Huang et al. (2025) for a Beijing HW showed that boundary-layer warming during the daytime was dominated by turbulent diffusion and was substantially enhanced under HW conditions, while at night turbulent diffusion became the dominant term as large-scale advective cooling weakened, with pronounced urban–rural differences. Our analysis offered a complementary perspective from the surface energy partitioning and turbulence diagnostics: the daytime enhancement of urban sensible heat and the increase in the Bowen ratio constituted the energy source for the strengthened turbulent diffusion, and the concentration of positive ΔTKE in the mid- to upper boundary layer suggested that processes such as entrainment might also be involved in the vertical redistribution of warming. At night, the sustained release of urban heat storage and anthropogenic heat maintained the additional warming in the near-surface layer; together with the weakened large-scale advective cooling reported by Huang et al. (2025), this could explain the persistence of nocturnal urban thermal anomalies during HWs. Tang et al. (2025) used wind-profiler observations in Beijing and found that subtropical-high-controlled HWs enhanced the PBL turbulence dissipation rate by about 55 %, with the near-surface layer driven mainly by buoyancy and the upper layers maintained primarily by wind shear. Our simulated urban ΔTKE, with positive values concentrated in the

https://doi.org/10.5194/egusphere-2026-3392
Preprint. Discussion started: 24 August 2026

mid- to upper boundary layer and weaker values near the surface, was physically consistent with such a vertical separation of buoyancy-driven near-surface and shear-maintained upper-layer turbulence: enhanced near-surface buoyancy rapidly exported turbulent energy upward, while wind shear allowed additional TKE to accumulate aloft. Our results further showed that this feature varied among LCZs, indicating a modulation by urban morphology. Sun et al. (2017) established the dominant role of heat storage in the HW surface energy budget, and Li et al. (2024) further demonstrated that urban thermal inertia drives the synoptic-scale persistence of urban temperatures; the present results extended this thermal-inertia mechanism from the surface to the boundary-layer column. Different LCZs appeared to influence the coupling strength between the stable boundary layer and the residual layer through their differing nocturnal heat-source supply and surface-roughness characteristics, thereby regulating the persistence of the residual-layer warm anomaly and the entrainment process during the following morning.

This study advanced the existing literature in three respects. First, it extended HW–UHI synergy to the vertical structure connecting the canopy and the boundary layer, revealing a time-dependent continuity and disruption in the upward transfer of additional warming. Second, it extended the LCZ perspective from traditional horizontal thermal-heterogeneity analysis to the vertical organisation of the boundary layer, showing that LCZ dependence was concentrated in the lower layers and gradually converged and weakened once the boundary-layer mean was taken. The influence of urban morphology on the HW response was thus best interpreted as a modulation of low-level coupling between thermodynamics and turbulence. Third, it extended the analysis of urban thermal anomalies from a single-day timescale to the day-to-day connection, showing that residual-layer thermal memory acted as a bridge between the previous day's heat storage and the next day's warming, with LCZ 1 retaining a ∼0.41 °C warm anomaly at 500–600 m through the night during HW1, while HW2 reproduced the same inter-LCZ ranking with a weaker absolute amplitude (Fig. S12).

Several limitations should be acknowledged. First, the analysis was based on typical HW cases and was therefore most representative of subtropical-high-controlled, quasi-stationary HWs. Coverage of different background weather regimes and a larger number of events is still limited, and the generalisability of the conclusions requires further verification. Second, the absolute urban PBLH, the height of the simulated turbulence maximum relative to the PBL top, and the precise upper extent of daytime vertical transport should be interpreted cautiously. This bias has little direct effect on BUHII because the common upper limit was set by the rural PBLH at 98.7 % of times, and the fixed-height Layer ΔT and $\Delta\Delta T$ diagnostics do not use PBLH as an input. Third, the number of grid cells in each LCZ sample was also not balanced; although connected-component screening was applied to ensure spatial homogeneity, the differences in sample size might still affect statistical robustness. Fourth, a limitation concerns the LCZ framework itself. The classical LCZ scheme (Level 0) (Stewart and Oke, 2012) assumes that building heights are approximately homogeneous within each class. This assumption can therefore underestimate the coupling between the urban canopy and the overlying boundary layer. In reality, the variability of building heights within an LCZ class is also a key control on the turbulence spectrum and on the way the urban fabric perturbs the vertical structure of the urban boundary layer (Mills et al., 2024; Yang et al., 2025). The WUDAPT community has been working towards more sophisticated representations of urban morphology that move beyond Level 0 to Level 1 and Level 2 schemes (Mills et al., 2024). Quantifying how within-class height variability modulates the vertical structure of HW-induced thermal anomalies, and testing whether such refined parameterisations alter the inter-LCZ contrasts identified in this study, will be an important direction for

https://doi.org/10.5194/egusphere-2026-3392
Preprint. Discussion started: 24 August 2026

future work. Fifth, the BUHII results were difficult to validate directly against observations, a limitation common to current urban boundary-layer research. We constrained the relevant model components through four complementary evaluations: (1) rural and CUR PBLH were compared with the harmonised PBLH product; (2) regional temperature and wind profiles were compared with Qingyuan IGRA soundings; (3) CUHII was compared with AWS observations; and (4) the observed inter-LCZ ranking of CUHII was used to evaluate the relative urban structure. The sounding evaluation supports the regional background vertical structure but cannot independently validate the urban-core profile, and the simulated CUHII remained slightly biased high. Because the core conclusions of this study were based on relative differences (HW relative to NHW; LCZ relative to CUR), systematic biases largely cancelled out in difference calculations. The qualitative and semi-quantitative conclusions concerning vertical non-uniformity, LCZ dependence, and surface energy partitioning were therefore relatively robust, whereas the absolute magnitudes should be interpreted with the model bias in mind and warrant further investigation. Sixth, Q_{F} was estimated using the residual method, which carries some uncertainty. Finally, although the regional-mean near-surface advection was of limited magnitude (Sect. 2.6), advective effects might exert a more pronounced modulation of the boundary-layer thermal structure under different synoptic backgrounds, and quantifying this in additional HW cases will be needed in future work.

5 Conclusions

This study examined how HWs modified the vertical structure of the UHI over the Guangzhou metropolitan area and how this response depended on LCZs, using 1 km LCZ-coupled WRF simulations with HW1 as the primary analysis and HW2 as a supplementary robustness check. Both CUHII and BUHII increased during HWs, but the additional warming was vertically non-uniform and strongest in the canopy and lower boundary layer. In the 30–100 m layer, the daily mean additional warming during HW1 was 0.54 °C in LCZ 1, 0.47 °C in LCZ 4, 0.43 °C in LCZ 2, and 0.28 °C in LCZ 6. The response extended into higher fixed-height layers during daytime boundary-layer development but contracted toward the surface at night, when the upper-level response weakened or reversed. LCZ contrasts in HW-induced additional warming were most evident below approximately 250 m: LCZ 1 showed the strongest response, LCZ 2 and LCZ 4 reached comparable warming through different energy–turbulence pathways, and LCZ 6 showed the weakest and shallowest response. LCZ 1 also retained a warm anomaly of up to approximately 0.41 °C at 500–600 m through the night during HW1.

Taken together, the results indicate a diurnally reorganised energy–turbulence–temperature chain. During the day, enhanced sensible heating, a higher Bowen ratio, and reduced low-level stability favoured the upward redistribution of near-surface warming as the boundary layer developed. At night, the sustained release of stored heat, the residual-method estimate of anthropogenic heat, and weaker low-level turbulence favoured the retention of additional warming in the lower layers. The persistence of the fixed-layer nocturnal anomaly further suggests a boundary-layer-scale thermal memory that can connect one day's urban heating to the following morning, with a strength that depends on urban morphology.

The decrease in HW-induced UHI amplification with height is consistent with the Shanghai simulations of Xin et al. (2024), whereas the nocturnal BUHII enhancement found here differs from their weak nocturnal response. This contrast points to a

https://doi.org/10.5194/egusphere-2026-3392
Preprint. Discussion started: 24 August 2026

possible modulation by synoptic regime, coastal circulation, and advection. These results extend the surface heat-storage and thermal-inertia mechanisms discussed by Sun et al. (2017) and Li et al. (2024) into the boundary-layer column and broaden LCZ analysis from horizontal canopy-temperature contrasts to the vertical organisation of urban thermal anomalies.

Confidence is highest in the relative HW–NHW and inter-LCZ contrasts and in the fixed-height lower-layer response. The exact urban PBLH and upper extent of daytime transport are less certain because the simulated CUR PBLH was high relative to the harmonised product, although the BUHII upper limit was almost always constrained by the better-reproduced rural PBLH. The results are also limited to two subtropical-high-controlled events in one metropolitan area, the LCZ sample sizes are unbalanced, and the residual estimate of Q_{F} is uncertain. Additional observations within the urban boundary layer and tests across other synoptic regimes, cities, and climate zones are needed to assess the generality of the inferred pathways.

These findings imply that near-surface UHII alone does not fully describe the atmospheric response of cities to HWs: the vertical extent, diurnal redistribution, and overnight persistence of urban thermal anomalies vary with urban morphology. By altering how deeply additional warming penetrates into the boundary layer, how long it persists overnight, and how much of the residual-layer anomaly is available for re-entrainment the following morning, urban form can influence the evolution of the urban atmosphere beyond the period of peak surface heating. Boundary-layer-resolved and LCZ-aware diagnostics can therefore improve the physical interpretation of urban extreme heat and provide a more complete basis for evaluating how urban morphology modifies the three-dimensional and multi-day atmospheric response to HWs.

Code and data availability. The hourly 2 m air temperature observations from automatic weather stations used in this study are obtained from the China Meteorological Administration (CMA) Data Service (http://data.cma.cn/en, last access: 11 May 2026). The harmonised global radiosonde-based PBLH dataset is publicly available from Guo et al. (2022) at https://doi.org/10.5281/zenodo.6498004. The Qingyuan radiosonde profiles are from the NOAA National Centers for Environmental Information Integrated Global Radiosonde Archive, Version 2 (Durre et al., 2016), available at https://doi.org/10.7289/V5X63K0Q (station WMO 59280; subset: July 2020; last access: 19 August 2026). The 2020 30 m annual China Land Cover Dataset is available from Yang and Huang (2026) at https://zenodo.org/records/18180184. The WUDAPT 100 m global LCZ dataset is available at https://doi.org/10.5281/zenodo.6364594 (Demuzere et al., 2022b), and the w2w tool used for coupling LCZ data into WRF is available at https://github.com/matthiasdemuzere/w2w (Demuzere et al., 2022a). The WRF model version 4.4 source code is available at https://github.com/wrf-model/WRF. The FNL 0.25° operational global analysis is available from the NCEP/NOAA Research Data Archive (https://doi.org/10.5065/D65Q4T4Z).

Author contributions. YY conceptualized the study and designed the experiments. FL wrote the original manuscript and plotted all the figures. FL, TS, ZZ, XB, GR, and SL assisted in the conceptualization and model development. All the authors contributed to the manuscript preparation, discussion, and writing.

Competing interests. The authors declare that they have no conflict of interest.

https://doi.org/10.5194/egusphere-2026-3392
Preprint. Discussion started: 24 August 2026

Acknowledgements. We acknowledge the High-Performance Computing Center of Nanjing University of Information Science & Technology for supporting this work.

Financial support. This study was supported by the National Natural Science Foundation of China (grant no. 42521006).

References

Ao, X., Wang, L., Zhi, X., Gu, W., Yang, H., and Li, D.: Observed Synergies between Urban Heat Islands and Heat Waves and Their Controlling Factors in Shanghai, China, Journal of Applied Meteorology and Climatology, 58, 1955–1972, https://doi.org/10.1175/JAMC-D-19-0073.1, 2019.

Brousse, O., Martilli, A., Foley, M., Mills, G., and Bechtel, B.: WUDAPT, an efficient land use producing data tool for mesoscale models? Integration of urban LCZ in WRF over Madrid, Urban Climate, 17, 116–134, https://doi.org/10.1016/j.uclim.2016.04.001, 2016.

Cao, Z., Wu, Z., Liu, L., Chen, Y., and Zou, Y.: Assessing the relationship between anthropogenic heat release warming and building characteristics in Guangzhou: A sustainable development perspective, Science of The Total Environment, 695, 133 759, https://doi.org/10.1016/j.scitotenv.2019.133759, 2019.

Chen, J., Dong, N., Liu, Z., Chen, Y., Luo, M., and Huang, H.: Local temperature impact of urban heat mitigation strategy based on WRF integrating urban canopy parameters and local climate zones, Building and Environment, 267, 112 257, https://doi.org/10.1016/j.buildenv.2024.112257, 2025.

Chew, L. W., Liu, X., Li, X.-X., and Norford, L. K.: Interaction between heat wave and urban heat island: A case study in a tropical coastal city, Singapore, Atmospheric Research, 247, 105 134, https://doi.org/10.1016/j.atmosres.2020.105134, 2021.

Ching, J., Mills, G., Bechtel, B., See, L., Feddema, J., Wang, X., Ren, C., Brousse, O., Martilli, A., Neophytou, M., Mouzourides, P., Stewart, I., Hanna, A., Ng, E., Foley, M., Alexander, P., Aliaga, D., Niyogi, D., Shreevastava, A., Bhalachandran, P., Masson, V., Hidalgo, J., Fung, J., Andrade, M., Baklanov, A., Dai, W., Milcinski, G., Demuzere, M., Brunsell, N., Pesaresi, M., Miao, S., Mu, Q., Chen, F., and Theeuwes, N.: WUDAPT: An Urban Weather, Climate, and Environmental Modeling Infrastructure for the Anthropocene, Bulletin of the American Meteorological Society, 99, 1907–1924, https://doi.org/10.1175/BAMS-D-16-0236.1, 2018.

Demuzere, M., Argüeso, D., Zonato, A., and Kittner, J.: W2W: A Python package that injects WUDAPT's LocalClimate Zone information in WRF, Journal of Open Source Software, 7, 4432, https://doi.org/10.21105/joss.04432, 2022a.

Demuzere, M., Kittner, J., Martilli, A., Mills, G., Moede, C., Stewart, I. D., Van Vliet, J., and Bechtel, B.: A global map of local climate zones to support earth system modelling and urban-scale environmental science, Earth System Science Data, 14, 3835–3873, https://doi.org/10.5194/essd-14-3835-2022, 2022b.

Durre, I., Yin, X., Vose, R. S., Applequist, S., Arnfield, J., Korzeniewski, B., and Hundermark, B.: Integrated Global Radiosonde Archive (IGRA), Version 2 [data set], Tech. rep., NOAA National Centers for Environmental Information, https://doi.org/10.7289/V5X63K0Q, 2016.

Gryning, S.-E., Batchvarova, E., Brümmer, B., Jørgensen, H., and Larsen, S.: On the extension of the wind profile over homogeneous terrain beyond the surface boundary layer, Boundary-Layer Meteorology, 124, 251–268, https://doi.org/10.1007/s10546-007-9166-9, 2007.

Guangdong Provincial Development and Reform Commission: Development plan for the Guangzhou metropolitan area, https://drc.gd.gov.cn/qtwj/content/post_4304004.html, 2023.

Guangzhou Municipal Planning and Natural Resources Bureau: Interpretation of Statistics on Urban Built-up Area of Guangzhou in 2020, https://ghzyj.gz.gov.cn/zwgk/xxgkml3/qt/tjsj/qt/content/post_7377912.html, 2021.

Guo, J., Zhang, J., and Shao, J.: A Harmonized Global Continental High-resolution Planetary Boundary Layer Height Dataset Covering 2017-2021 [data set], Tech. rep., Zenodo, https://doi.org/10.5281/zenodo.6498004, 2022.

https://doi.org/10.5194/egusphere-2026-3392
Preprint. Discussion started: 24 August 2026

Guo, J., Zhang, J., Shao, J., Chen, T., Bai, K., Sun, Y., Li, N., Wu, J., Li, R., Li, J., Guo, Q., Cohen, J. B., Zhai, P., Xu, X., and Hu, F.: A merged continental planetary boundary layer height dataset based on high-resolution radiosonde measurements, ERA5 reanalysis, and GLDAS, Earth System Science Data, 16, 1–14, https://doi.org/10.5194/essd-16-1-2024, 2024.

Holtslag, A. a. M. and Moeng, C.-H.: Eddy Diffusivity and Countergradient Transport in the Convective Atmospheric Boundary Layer, https://journals.ametsoc.org/view/journals/atsc/48/14/1520-0469_1991_048_1690_edacti_2_0_co_2.xml, 1991.

Huang, Q., Zhang, Y., Xin, J., Li, Y., Qin, Y., and Wang, L.: Atmospheric boundary layer heat budget and its urban-rural differences in Beijing during a heatwave event, Atmospheric Research, 325, 108 243, https://doi.org/10.1016/j.atmosres.2025.108243, 2025.

IPCC: Global Warming of 1.5 °C, Tech. rep., World Meteorological Organization, Geneva, Switzerland, https://www.ipcc.ch/sr15/, 2018.

Jiang, S., Lee, X., Wang, J., and Wang, K.: Amplified Urban Heat Islands during Heat Wave Periods, Journal of Geophysical Research: Atmospheres, 124, 7797–7812, https://doi.org/10.1029/2018JD030230, 2019.

Kabisch, N., Remahne, F., Ilsemann, C., and Fricke, L.: The urban heat island under extreme heat conditions: a case study of Hannover, Germany, Scientific Reports, 13, 23 017, https://doi.org/10.1038/s41598-023-49058-5, 2023.

Kato, S. and Yamaguchi, Y.: Analysis of urban heat-island effect using ASTER and ETM+ Data: Separation of anthropogenic heat discharge and natural heat radiation from sensible heat flux, Remote Sensing of Environment, 99, 44–54, https://doi.org/10.1016/j.rse.2005.04.026, 2005.

Kong, J., Zhao, Y., Carmeliet, J., and Lei, C.: Urban Heat Island and Its Interaction with Heatwaves: A Review of Studies on Mesoscale, Sustainability, 13, 10 923, https://doi.org/10.3390/su131910923, 2021.

Kotharkar, R. and Ghosh, A.: Review of heat wave studies and related urban policies in South Asia, Urban Climate, 36, 100 777, https://doi.org/10.1016/j.uclim.2021.100777, 2021.

Kuang, M., Zheng, Y., Deng, X., Yang, Y., Wang, J., Sui, X., and Peng, Y.: Flood risk management in planning and construction of city: the Guangzhou experience, Proceedings of IAHS, 386, 277–283, https://doi.org/10.5194/piahs-386-277-2024, 2024.

Li, D. and Bou-Zeid, E.: Synergistic Interactions between Urban Heat Islands and Heat Waves: The Impact in Cities Is Larger than the Sum of Its Parts, Journal of Applied Meteorology and Climatology, 52, 2051–2064, https://doi.org/10.1175/JAMC-D-13-02.1, 2013.

Li, D., Sun, T., Liu, M., Wang, L., and Gao, Z.: Changes in Wind Speed under Heat Waves Enhance Urban Heat Islands in the Beijing Metropolitan Area, Journal of Applied Meteorology and Climatology, 55, 2369–2375, https://doi.org/10.1175/JAMC-D-16-0102.1, 2016.

Li, D., Wang, L., Liao, W., Sun, T., Katul, G., Bou-Zeid, E., and Maronga, B.: Persistent urban heat, Science Advances, 10, https://doi.org/10.1126/sciadv.adj7398, 2024.

Li, X., Wang, L., Chen, D., Yang, K., Xue, B., and Sun, L.: Near-surface air temperature lapse rates in the mainland China during 1962–2011, Journal of Geophysical Research: Atmospheres, 118, 7505–7515, https://doi.org/10.1002/jgrd.50553, 2013.

Li, X., Hang, J., Mo, Z., and Wang, Q.: Impact of adjacent city development on the urban heat island intensity and thermal stress : A WRF-BEP/BEM and LCZ-integrated assessment, Building and Environment, 289, 114 024, https://doi.org/10.1016/j.buildenv.2025.114024, 2026.

Luo, F., Yang, Y., Zong, L., and Bi, X.: The interactions between urban heat island and heat waves amplify urban warming in Guangzhou, China: Roles of urban ventilation and local climate zones, Frontiers in Environmental Science, 11, 1084 473, https://doi.org/10.3389/fenvs.2023.1084473, 2023.

Martilli, A., Clappier, A., and Rotach, M. W.: An Urban Surface Exchange Parameterisation for Mesoscale Models, Boundary-Layer Meteorology, 104, 261–304, https://doi.org/10.1023/A:1016099921195, 2002.

https://doi.org/10.5194/egusphere-2026-3392
Preprint. Discussion started: 24 August 2026

Meehl, G. A. and Tebaldi, C.: More Intense, More Frequent, and Longer Lasting Heat Waves in the 21st Century, Science, 305, 994–997, https://doi.org/10.1126/science.1098704, 2004.

Mills, G., Arunachalam, S., Shi, Y., and Baklanov, A.: Jason Ching and the development of an Urban Climate Science: An introduction to the special issue on the World Urban Database Access Portal Tools (WUDAPT), Urban Climate, 58, 102 179, https://doi.org/10.1016/j.uclim.2024.102179, 2024.

Molnár, G., Gyöngyösi, A. Z., and Gál, T.: Integration of an LCZ-based classification into WRF to assess the intra-urban temperature pattern under a heatwave period in Szeged, Hungary, Theoretical and Applied Climatology, 138, 1139–1158, https://doi.org/10.1007/s00704-019-02881-1, 2019.

National Centers for Environmental Prediction, National Weather Service, NOAA, U.S. Department of Commerce: NCEP GDAS/FNL 0.25 Degree Global Tropospheric Analyses and Forecast Grids, https://doi.org/10.5065/D65Q4T4Z, 2015.

Ngarambe, J., Nganyiyimana, J., Kim, I., Santamouris, M., and Yun, G. Y.: Synergies between urban heat island and heat waves in Seoul: The role of wind speed and land use characteristics, PLOS ONE, 15, e0243 571, https://doi.org/10.1371/journal.pone.0243571, 2020.

Oke, T. R.: Boundary Layer Climates, Routledge, London, 2nd edn., https://doi.org/10.4324/9780203407219, 2002.

Oke, T. R., Mills, G., Christen, A., and Voogt, J. A.: Urban Climates, Cambridge University Press, Cambridge, UK, https://doi.org/10.1017/9781139016476, 2017.

Park, K. and Baik, J.-J.: Diurnal evolution of synergistic interactions between urban heat islands and heat waves: An extreme heat wave case study in Seoul, South Korea, Weather and Climate Extremes, 51, 100 854, https://doi.org/10.1016/j.wace.2026.100854, 2026.

Richard, Y., Pohl, B., Rega, M., Pergaud, J., Thevenin, T., Emery, J., Dudek, J., Vairet, T., Zito, S., and Chateau-Smith, C.: Is Urban Heat Island intensity higher during hot spells and heat waves (Dijon, France, 2014–2019)?, Urban Climate, 35, 100 747, https://doi.org/10.1016/j.uclim.2020.100747, 2021.

Robine, J.-M., Cheung, S. L. K., Le Roy, S., Van Oyen, H., Griffiths, C., Michel, J.-P., and Herrmann, F. R.: Death toll exceeded 70,000 in Europe during the summer of 2003, Comptes Rendus. Biologies, 331, 171–178, https://doi.org/10.1016/j.crvi.2007.12.001, 2007.

Rotach, M. W., Vogt, R., Bernhofer, C., Batchvarova, E., Christen, A., Clappier, A., Feddersen, B., Gryning, S.-E., Martucci, G., Mayer, H., Mitev, V., Oke, T. R., Parlow, E., Richner, H., Roth, M., Roulet, Y.-A., Ruffieux, D., Salmond, J. A., Schatzmann, M., and Voogt, J. A.: BUBBLE – an Urban Boundary Layer Meteorology Project, Theoretical and Applied Climatology, 81, 231–261, https://doi.org/10.1007/s00704-004-0117-9, 2005.

Salamanca, F., Krpo, A., Martilli, A., and Clappier, A.: A new building energy model coupled with an urban canopy parameterization for urban climate simulations—part I. formulation, verification, and sensitivity analysis of the model, Theoretical and Applied Climatology, 99, 331–344, https://doi.org/10.1007/s00704-009-0142-9, 2010.

Schlünzen, K. H., Grimmond, S., and Baklanov, A.: Guidance on Measuring, Modelling and Monitoring the Canopy Layer Urban Heat Island (CL-UHI), Tech. Rep. WMO-No. 1292, World Meteorological Organization, Geneva, Switzerland, ISBN 978-92-63-11292-2, https://library.wmo.int/idurl/4/58410, 2023.

Seidel, D. J., Zhang, Y., Beljaars, A., Golaz, J., Jacobson, A. R., and Medeiros, B.: Climatology of the planetary boundary layer over the continental United States and Europe, Journal of Geophysical Research: Atmospheres, 117, 2012JD018 143, https://doi.org/10.1029/2012JD018143, 2012.

Shi, T., Yang, Y., Jiang, Y., Xun, S., and Zhang, A.: Impact of the variation of urban heat island intensity on temperature series in Anhui Province, Climatic and Environmental Research, 16, 779–788, https://doi.org/10.3878/j.issn.1006-9585.2011.06.13, in Chinese, 2011.

Skamarock, W. C., Klemp, J. B., Dudhia, J., Gill, D. O., Liu, Z., Berner, J., Wang, W., Powers, J. G., Duda, M. G., Barker, D. M., and Huang, X.-Y.: A Description of the Advanced Research WRF Model Version 4, NCAR Technical Note NCAR/TN-556+STR, National Center for Atmospheric Research, Boulder, Colorado, USA, https://doi.org/10.5065/1dfh-6p97, 2019.

Stewart, I. D. and Oke, T. R.: Local Climate Zones for Urban Temperature Studies, Bulletin of the American Meteorological Society, 93, 1879–1900, https://doi.org/10.1175/BAMS-D-11-00019.1, 2012.

Stull, R. B.: An Introduction to Boundary Layer Meteorology, Kluwer Academic Publishers, Dordrecht, the Netherlands, https://doi.org/10.1007/978-94-009-3027-8, 1988.

Sun, T., Kotthaus, S., Li, D., Ward, H. C., Gao, Z., Ni, G.-H., and Grimmond, C. S. B.: Attribution and mitigation of heat wave-induced urban heat storage change, Environmental Research Letters, 12, 114 007, https://doi.org/10.1088/1748-9326/aa922a, 2017.

Tan, J., Zheng, Y., Song, G., Kalkstein, L. S., Kalkstein, A. J., and Tang, X.: Heat wave impacts on mortality in Shanghai, 1998 and 2003, International Journal of Biometeorology, 51, 193–200, https://doi.org/10.1007/s00484-006-0058-3, 2007.

Tang, N., Guo, J., Chen, J., Li, Z., Guo, X., Sun, Y., Xu, H., Zhang, Z., Li, N., Zeng, L., Yu, M., and Chen, T.: Anticyclone Driven Heat Waves Intensify Beijing's Urban Boundary-Layer Turbulence, Geophysical Research Letters, 52, e2025GL115 800, https://doi.org/10.1029/2025GL115800, 2025.

The People' s Government of Guangzhou Municipality: Seventh national population census bulletin of Guangzhou, https://www.gz.gov.cn/zwgk/sjfb/tjgb/content/post_7286268.html, 2021.

Tian, W., Yang, Y., Wang, L., Zong, L., Zhang, Y., and Liu, D.: Role of local climate zones and urban ventilation in canopy urban heat island–heatwave interaction in Nanjing megacity, China, Urban Climate, 49, 101 474, https://doi.org/10.1016/j.uclim.2023.101474, 2023.

Wang, Z., Xiao, Z., Tam, C.-Y., Pan, W., Chen, J., Hu, C., Ren, C., Wei, W., and Yang, S.: The projected effects of urbanization and climate change on summer thermal environment in Guangdong-Hong Kong-Macao Greater Bay Area of China, Urban Climate, 37, 100 866, https://doi.org/10.1016/j.uclim.2021.100866, 2021.

WMO and WHO: Heatwaves and Health: Guidance on Warning-System Development, Tech. Rep. WMO-No. 1142, World Meteorological Organization and World Health Organization, Geneva, Switzerland, https://www.who.int/publications/m/item/heatwaves-and-health--guidance-on-warning-system-development, 2016.

Xin, J., Zhang, Y., Bai, W., and Song, Z.: Response of urban heat island effects within the planetary boundary layer to heat waves and impact of horizontal advection over Shanghai, Atmospheric Research, 311, 107 721, https://doi.org/10.1016/j.atmosres.2024.107721, 2024.

Yang, J. and Huang, X.: The 30 m annual land cover dataset and its dynamics in China from 1990 to 2019, Earth System Science Data, 13, 3907–3925, https://doi.org/10.5194/essd-13-3907-2021, 2021.

Yang, J. and Huang, X.: The 30 m annual land cover datasets and its dynamics in China from 1985 to 2025 [data set], Tech. rep., Zenodo, https://doi.org/10.5281/zenodo.18180184, 2026.

Yang, J., Yu, W., Baklanov, A., He, B., and Ge, Q.: Mainstreaming the local climate zone framework for climate-resilient cities, Nature Communications, 16, 5705, https://doi.org/10.1038/s41467-025-61394-w, 2025.

Yang, Y., Luo, F., Xue, J., Zong, L., Tian, W., and Shi, T.: Research progress and prospects of the synergistic effects of urban heat waves and canopy urban heat island, Advances in Earth Science, 39, 331–346, https://doi.org/10.11867/j.issn.1001-8166.2024.032, in Chinese, 2024.

Zhao, L., Lee, X., Smith, R. B., and Oleson, K.: Strong contributions of local background climate to urban heat islands, Nature, 511, 216–219, https://doi.org/10.1038/nature13462, 2014.

https://doi.org/10.5194/egusphere-2026-3392
Preprint. Discussion started: 24 August 2026

Zhou, Y., Weng, Q., Gurney, K. R., Shuai, Y., and Hu, X.: Estimation of the relationship between remotely sensed anthropogenic heat discharge and building energy use, ISPRS Journal of Photogrammetry and Remote Sensing, 67, 65–72, https://doi.org/10.1016/j.isprsjprs.2011.10.007, 2012.

Zong, L., Liu, S., Yang, Y., Ren, G., Yu, M., Zhang, Y., and Li, Y.: Synergistic Influence of Local Climate Zones and Wind Speeds on the Urban Heat Island and Heat Waves in the Megacity of Beijing, China, Frontiers in Earth Science, 9, 673 786, https://doi.org/10.3389/feart.2021.673786, 2021.